

Technische Universität München  
Fakultät für Physik  
Walther-Meißner-Institut für Tieftemperaturforschung

**Bachelor's Thesis in Physics**

# Finite Size Effects of the Anisotropic Magnetoresistance

Manuel Müller

August 11, 2017

Supervisor: Dr. Matthias Althammer  
Primary Reviewer: Prof. Dr. Rudolf Gross

Primary Reviewer: Prof. Dr. Rudolf Gross

Secondary Reviewer: Prof. Dr. Aliaksandr Bandarenka

# Contents

<b>Abstract</b> . . . . .	ix
<b>1 Introduction</b> . . . . .	1
<b>2 Theoretical background</b> . . . . .	5
2.1 Charge and spin currents . . . . .	5
2.2 Spin-dependent transverse velocity . . . . .	6
2.2.1 Spin-orbit interaction (SOI) . . . . .	6
2.2.2 Extrinsic effects . . . . .	8
2.2.3 Intrinsic effects . . . . .	8
2.2.4 Spin Hall effect (SHE) and its inverse (ISHE) . . . . .	9
2.2.5 Anomalous Hall effect (AHE) . . . . .	10
2.3 Angle dependent magnetoresistance (ADMR) effects . . . . .	13
2.3.1 Spin Hall magnetoresistance (SMR) . . . . .	13
2.3.2 Angle-dependent contribution of the AHE . . . . .	15
2.3.3 Anisotropic magnetoresistance (AMR) . . . . .	17
<b>3 Experimental techniques</b> . . . . .	19
3.1 Sample fabrication . . . . .	19
3.1.1 Work at the ultra-high Vacuum (UHV) Cluster . . . . .	19
3.1.2 Final steps . . . . .	20
3.2 Procedure of the ADMR measurement . . . . .	21
3.2.1 The "Moria"-cryostat . . . . .	21
3.2.2 Definition of the different measurement geometries . . . . .	22
<b>4 Results and discussion</b> . . . . .	23
4.1 Finite size effects of the anisotropic magnetoresistance . . . . .	23
4.1.1 Data evaluation . . . . .	23
4.1.2 Thickness-dependent behaviour of the resistivity . . . . .	27
4.1.3 In-plane-results . . . . .	28
4.1.4 Oopt-results . . . . .	30
4.1.5 Oopj-results . . . . .	31
4.1.6 Investigation of the possible contribution of higher order AMR-contributions . . . . .	32
4.2 Scaling behaviour of the anomalous Hall effect . . . . .	34
4.2.1 Experimental determination of the transverse resistivity contribution of the AHE . . . . .	34
4.2.2 Thickness-dependent behaviour . . . . .	35
4.2.3 Experimental scaling behaviour . . . . .	35
4.3 Unidirectional spin Hall magnetoresistance . . . . .	38
4.3.1 Theoretical background . . . . .	38
4.3.2 Additional ADMR-measurements . . . . .	39
4.3.3 Attempts to detect the USMR in the Co Pt-boundary layer . . . . .	42

<b>5 Summary</b> . . . . .	47
5.1 Conclusion and outlook . . . . .	47
<b>A Details</b> . . . . .	51
A.1 Bonding scheme . . . . .	51
A.2 Hall-bar pads used for ADMR-measurements . . . . .	51
A.3 Fabricated samples . . . . .	52
A.4 Used abbreviations . . . . .	53
<b>B Possible influence of a tilt on AMR-amplitude in oopj-geometry</b> . .	55
<b>C ADMR-results of the Co Pt-sample</b> . . . . .	59
<b>D Application of the differential resistance <math>r</math> to detect the USMR</b> . . .	61
<b>Bibliography</b> . . . . .	65
<b>Acknowledgements</b> . . . . .	69

# List of Figures

1.1	"Murphy's take on Moore's law."	1
2.1	Charge- and spin currents	6
2.2	Semiclassical model of the spin-orbit interaction	7
2.3	Illustration of the extrinsic spin-dependent transverse velocity effects	8
2.4	Illustration of the intrinsic spin-dependent transverse velocity effect	9
2.5	Spin Hall effect and its inverse	10
2.6	Density of states of the 3d and 4s states in the ferromagnetic nickel as well as the paramagnetic cooper	11
2.7	Schematic representation of the AHE	11
2.8	The transverse Hall effect behaviour of a 100 nm thin Fe <sub>3</sub> O <sub>4</sub> film measured at 200 K	12
2.9	Scaling behaviour of the transverse conductivity due to the AHE	13
2.10	Illustration of the SMR-effect in a NM-FMI-interface	15
2.11	Depiction of the angle-dependent resistivity contribution of the AHE	16
2.12	Plot of the normalized longitudinal resistivity as a function of the distance t between the spin accumulations	16
2.13	Common magnetic field dependence of the resistivity of a ferromagnetic conductor	17
2.14	Schematic representation of the origin of the AMR	18
3.1	Schematic representation of the UHV Cluster	20
3.2	Microscope image of a finished sample	21
3.3	Illustration of the Hall-bar measurement geometry	21
3.4	Depiction of the Hall-bar measurement geometries	22
3.5	Schematic representation of the orientation of the external magnetic field with respect to the chip carrier system of the dipstick in the Moria Cryostat in ip- and oop-geometry	22
4.1	Expected behaviour of $\rho_{\text{long}}$ due to the AMR for $\rho_1 > 0$ in the three possible measurement geometries	24
4.2	Expected behaviour of $\rho_{\text{trans}}$ for $\rho_1 > 0, \rho_2 < 0$ due to the AMR in the three possible measurement geometries	24
4.3	Exemplary measured longitudinal ADMR behaviour of the resistivity in each of the three possible measurement geometries	25
4.4	Exemplary measured transverse ADMR behaviour of the resistivity in each of the three possible measurement geometries	26
4.5	Measured mean value of the longitudinal resistivity of both Hall-bars as a function of the layer thickness	27
4.6	Dependence of the longitudinal and transverse AMR-amplitude in ip-geometry of the layer thickness	28
4.7	Difference of the longitudinal and transverse in-plane AMR-amplitudes as a function of the external field for three samples of different thickness	29

4.8	Behaviour of the longitudinal changes of resistivity amplitude due to the AMR-effect in oopt-geometry as a function of the layer thickness $d$ . . . . .	30
4.9	Behaviour of the longitudinal changes of resistivity amplitude in oopj-geometry as a function of the layer thickness . . . . .	31
4.10	Comparison of the longitudinal relative changes of resistivity amplitude in ip- and oopt-geometry as a function of the layer thickness . . . . .	33
4.11	Exemplary depiction of the measured anomalous Hall effect for both oopj and oopt-geometry . . . . .	34
4.12	Experimental behaviour of the resistivity contribution of the AHE $\rho_{\text{AHE}}$ as a function of the layer thickness $d$ of the samples in both oopj and oopt geometry . . . . .	35
4.13	Experimental behaviour of the transverse conductivity due to the anomalous Hall effect $\sigma_{\text{AHE}}$ as a function of $\sigma_{\text{long}}$ in oopj and oopt geometry . . . . .	36
4.14	Anomalous Hall angle $\frac{\sigma_{\text{AHE}}}{\sigma_{\text{long}}}$ as a function of the layer thickness $d$ . . . . .	37
4.15	Behaviour of the longitudinal changes of the resistivity amplitude in oopj-geometry at 7T as a function of the layer thickness of the samples together with an adapted theory curve . . . . .	38
4.16	Illustration of the USMR in a Pt Co-interface layer . . . . .	39
4.17	Behaviour of the longitudinal changes of resistivity amplitude due to the AMR-effect in oopt-geometry as a function of the layer thickness of the co-samples as well as the Co Pt-sample . . . . .	40
4.18	Behaviour of the longitudinal changes of resistivity amplitude in oopj-geometry at 7 T as a function of the layer thickness of the co-samples as well as the Co Pt-sample . . . . .	41
4.19	Behaviour of the longitudinal changes of resistivity amplitude in ip-geometry as a function of the layer thickness of the Co-samples as well as the Co Pt-sample . . . . .	41
4.20	In-plane ADMR-measurement results of (Ga,Mn)As epilayers at an applied current of $\pm 300 \mu\text{A}$ , 0.5 T and 130 K . . . . .	43
4.21	$V_{\text{avg}}$ as a function of the angle $\alpha$ in longitudinal and transverse direction.	44
4.22	$E_{\text{diff}}$ as a function of the angle $\alpha$ in longitudinal and transverse direction	45
5.1	Scheme of the magnetization-switching device fabricated by Miron et. al.	49
A.1	Standard bonding scheme applied in this thesis. . . . .	51
B.1	Simulated oopj-behaviour for a tilt of $\alpha = 5^\circ$ with $\rho_0 = 1$ and $\rho_1 = 0.02$	56
B.2	Simulated oopj-behaviour for a tilt of $\gamma = 5^\circ$ with $\rho_0 = 1$ and $\rho_1 = 0.02$	56
B.3	Simulated oopj-behaviour for a tilt of both $\gamma = 4^\circ$ and $\alpha = 4^\circ$ with $\rho_0 = 1$ and $\rho_1 = 0.02$ . . . . .	57
C.1	Measured longitudinal ADMR behaviour of the resistivity of the Co Pt-sample in each of the three possible measurement geometries . . . . .	59
C.2	Measured transverse ADMR behaviour of the resistivity of the Co Pt-sample in each of the three possible measurement geometries . . . . .	59
D.1	Differential resistance of the Co Pt-sample as a function of the angle $\alpha$ for both current polarities. . . . .	62
D.2	Curvature $\kappa$ of the Co Pt-sample as a function of the angle $\alpha$ for positive current polarity. . . . .	62

# List of Tables

4.1	Mathematical expression of the magnetization vector in the three different measurement geometries . . . . .	23
4.2	Theoretical ADMR-behaviour of $\rho_{\text{long}}$ and $\rho_{\text{trans}}$ in the three possible measurement geometries . . . . .	39
A.1	Standard Hall pads used in ADMR-measurements . . . . .	51
A.2	List of fabricated samples and particularities that occurred at their fabrication . . . . .	52
A.3	Used abbreviations in order of their appearance . . . . .	53





# Abstract

Conventional electronic devices use the electronic charge of electrons to transport and store data. Due to the constantly growing demand of modern technology on the power, speed and data processing of said devices, they are approaching their technological limit due to Joule heating. The application of spin currents instead of charge currents, investigated in the field of spintronics, might offer a solution to this problem. One effect that has already found technological relevance in magnetical sensors is the anisotropic magnetoresistance (AMR). This thesis investigates the relation of the amplitudes of the angle-dependent changes in resistivity of a thin-film ferromagnetic conductor due to the AMR to its layer thickness  $d$  as well as the conductivity-dependent scaling behaviour of the anomalous Hall effect (AHE), which is another spin-current based effect in ferromagnetic conductors. For this reason angle-dependent magnetotransport measurements in an external magnetic field were conducted on Hall-bar mesa structures containing layers of the ferromagnet cobalt with varying thickness. The dependence of the amplitude of the AMR on said layer thickness has been extracted from these measurements for different measurement geometries. Taking the extracted data into account, a possible additional contribution of the AHE on the longitudinal resistivity is discussed. Furthermore, the behaviour of the transverse conductivity  $\sigma_{\text{AHE}}$  due to the AHE depending on the longitudinal conductivity  $\sigma_{\text{long}}$  was analyzed and can be attributed to different scaling regimes. Both the range and proportionality factor to  $\sigma_{\text{AHE}}$  of said regimes have been quantified and compared to previous experimental results. Additionally, we investigated whether the recently discovered unidirectional spin Hall magnetoresistance (USMR) in ferromagnet-nonmagnet-interfaces can be detected in a cobalt|platinum bilayer with a Hall-bar geometry.



# Chapter 1

## Introduction

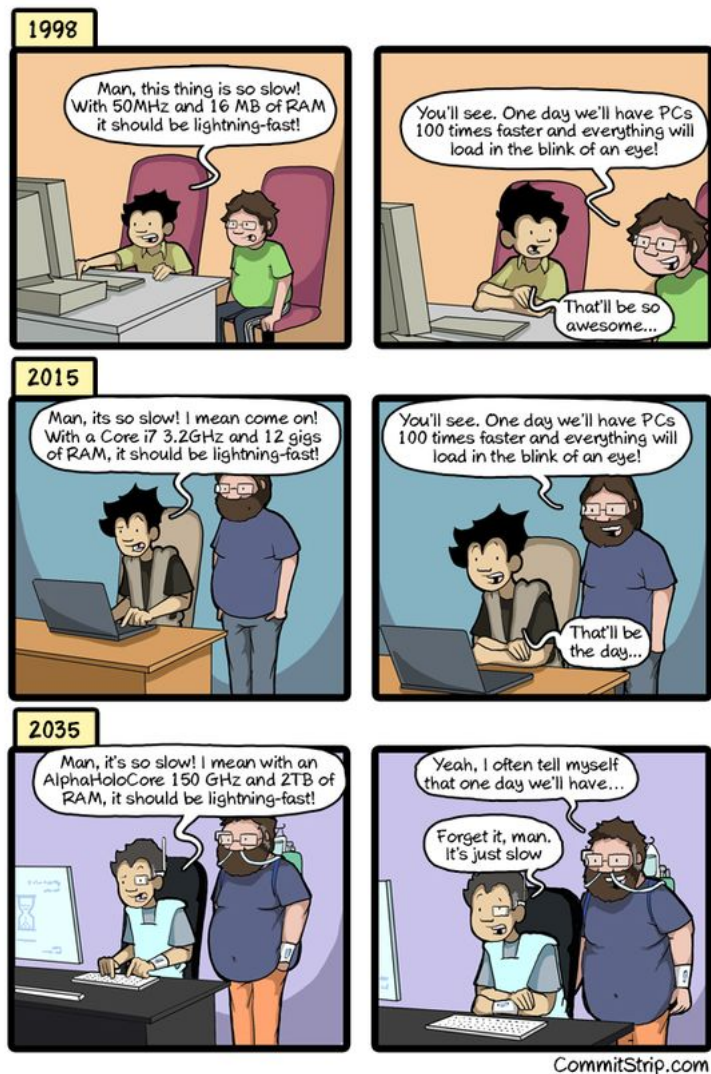


Figure 1.1: "Murphy's take on Moore's law." Taken from [1].

Fig. 1.1 depicts two friends discussing the operational speed of their computer at three different times in the past, present and near future. Each time they are faced with the problem of low loading-velocity of their present computer. While one of them remains optimistic and encourages his friend that in the future with much faster and more powerful PCs everything will load in "the blink of an eye", the other one grows more pessimistic over time as even though his friend's prediction has come true, he is still faced with the same problem of low loading-velocity. Funnily enough, the only

thing that changes between the different times apart from the appearance of the two friends are the amounts of RAM as well as the frequency of the processor of their present computer. However, as computer programs evolve in the same manner as computers, they become more complex and advanced. Therefore, regardless of the power of their current PC, the two friends are always stuck with the same old problem of low processing speed of their computer that we all know only too well.

This cartoon illustrates how much increasing computer capacity over time is taken for granted and how little the scientific and engineering work required to enable this tremendous development is appreciated. In the past this growth could be approximately described by Moore's Law [2] which states that the number of transistors, that can be integrated into a single computer chip doubles within two years of research. For the past decade it has been accurately describing the development of the processing power of PCs. However, this development requires the processor architecture size to decrease dramatically over time culminating in Intel's latest breakthrough in September 2014 with a process length of 14 nm [3]. Since this date no further size reduction has been achieved due to Joule heating of charge currents limiting the downscaling [4], possibly marking the end of the validity of Moore's Law [5].

One possible solution for this problem is the transport of angular momentum via spin currents in contrast to the flow of charges in charge currents as they are predicted to be dissipationless and less restricted by heating [6]. The research field investigating the formation and manipulation of said spin currents as well as how to combine them with charge currents to improve existing technology, is called spintronics [7]. Particularly the conversion of charge currents into spin currents via the spin Hall effect (SHE) [8] and vice versa via the inverse spin Hall effect (ISHE) [9] in paramagnetic conductors as well as the emergence of spin-polarized currents caused by the anomalous Hall effect (AHE) [10] in ferromagnetic conductors hold great promise for the fabrication of spin-based devices e.g. spin transistors [11] to reestablish the validity of Moore's Law. While offering these fascinating possibilities for future applications, one spintronics effect has already found its technological application, namely the anisotropic magnetoresistance (AMR)[12] in ferromagnetic conductors. It was first applied in early hard drives for disk read heads [13, 14]. While nowadays disk read heads work due to the giant magnetoresistance (GMR) [15] and the tunneling magnetoresistance (TMR) [16], the AMR has "paved the way" [17] for the quick development of GMR and TMR sensors and is nowadays still used in a wide array of magnetic field sensors [14].

This bachelor thesis aims to expand on the knowledge of the well understood AMR effect by investigating its size effect in thin film ferromagnetic samples as well as on the AHE which is still of vast scientific interest, by examining its scaling behaviour and potential influence on the resistivity of ferromagnetic conductors dependent on their geometry and magnetization orientation. Additionally, this thesis illustrates a first attempt at the Walther-Meißner-Institute to detect and quantify the recently discovered unidirectional spin Hall magnetoresistance (USMR), occurring at the interface of a heavy nonmagnetic conductor and a magnetic conductor in a cobalt|platinum bilayer with the normal Hall-bar geometry. In **chapter 2**, a quick overview on the definition and interplay mechanisms of charge currents and spin currents as well as an explanation of the origin of the AMR and AHE are given. **Chapter 3** delivers insight in how the thin film ferromagnetic samples in this thesis have been fabricated. In **chapter 4**, the obtained data are presented and discussed. Firstly, the measured size effect of the AMR

---

is described. Afterwards, the scaling behaviour of the AHE is determined and compared to previous experimental results. Furthermore, it will be investigated up to what extent its resistivity contribution has influenced the AMR-results. At last, the first steps taken in the investigation of the USMR effect are illustrated. Finally, **chapter 5** at first gives a quick summary of the most important results and then closes with an outlook on further experiments that should be conducted in this field and illustrates possibilities for future applications of the investigated effects.



# Chapter 2

## Theoretical background

This chapter is dedicated to charge and spin currents as well as how their interplay can cause many fascinating effects in magnetic as well as non-magnetic conductors. In the beginning, a general definition of the terms "charge currents" and "spin currents" will be given. Afterwards, we will look into the microscopic mechanisms that lead to said interplay mechanisms between the two current types via spin-orbit interaction. Subsequently, it will be shown how these mechanisms can give rise to effects such as the spin Hall effect, the inverse spin Hall effect in paramagnets as well as the anomalous Hall effect in ferromagnets. At last, a general review on how to utilize and measure these effects via angle-dependent changes of the electrical resistance in an external magnetic field will be given. Among those are the spin hall magnetoresistance (SMR) in non-magnetic conductors and the anisotropic magnetoresistance (AMR) in magnetic conductors. In the latter, the anomalous Hall effect can also give rise to an additional contribution to the resistance.

### 2.1 Charge and spin currents

A conventional electric current consists of electrons that carry an electric charge  $q = -e$  as well as a spin  $\mathbf{s}$ <sup>1</sup>. Making use of a two spin channel model, separating the charge current into spin up ( $\uparrow$ ) and spin down ( $\downarrow$ ) channels one can intuitively write the conventional charge current density as the sum of the up ( $\mathbf{J}_{\uparrow}$ ) and spin down ( $\mathbf{J}_{\downarrow}$ ) charge current densities [18]:

$$\mathbf{J}_q = \mathbf{J}_{\uparrow} + \mathbf{J}_{\downarrow} \quad (2.1)$$

In addition, one can define the spin current density  $\mathbf{J}_s$  as a flow of spin angular momentum by taking the difference of  $\mathbf{J}_{\uparrow}$  and  $\mathbf{J}_{\downarrow}$  [18]:

$$\mathbf{J}_s = -\frac{\hbar}{2e}(\mathbf{J}_{\uparrow} - \mathbf{J}_{\downarrow}) \quad (2.2)$$

Here  $e$  is the elementary charge  $e > 0$  and  $\hbar$  is the reduced Planck constant.<sup>2</sup> With these two equations in mind, two special cases should be considered. The conventional unpolarized charge current ( $\mathbf{J}_s = 0$ ) is described as  $\mathbf{J}_{\uparrow} = \mathbf{J}_{\downarrow}$  [see Fig. 2.1a)], while  $\mathbf{J}_{\uparrow} = -\mathbf{J}_{\downarrow}$  yields a pure spin current. Since an equal amount of spin up and spin down electrons are moving in opposite directions,  $\mathbf{J}_q$  vanishes [see Fig. 2.1(c)]. Apart from these two extreme cases, a spin-polarized charge current can be described with  $\mathbf{J}_{\uparrow} \neq \mathbf{J}_{\downarrow}$  [see Fig. 2.1(b)]. Here, neither of the both current types vanishes [18].

---

<sup>1</sup>In the course of this thesis, the symbol  $\mathbf{s}$  always stands for the orientation of the majority spins in a two spin channel model.

<sup>2</sup>  $\hbar = 1.054571800(13) \cdot 10^{-34} \text{Js}$

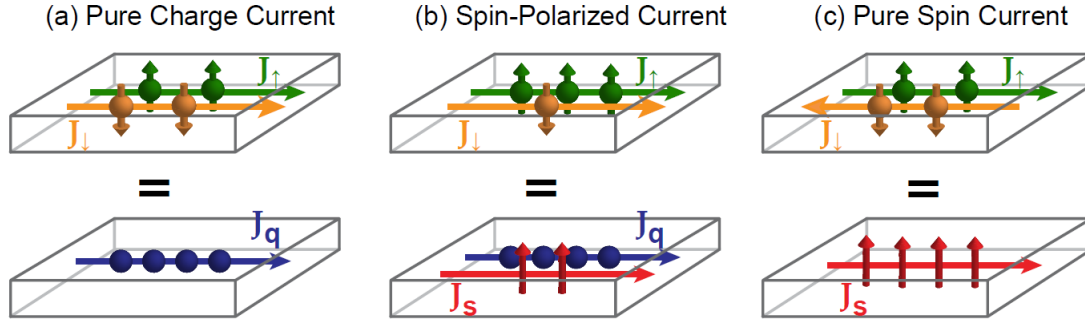


**Figure 2.1:** Two spin channel model illustration of a pure charge current (a), with no net transported spin polarization, a spin-polarized charge current (b) that carries both spin and charge and a pure spin current (c), where the charge carriers with different spin orientations move in opposite directions, such that the total charge current vanishes. Taken from [18].

Even though charge and spin currents can be described very analogously, one must consider that only the charge of the electrons is a conserved transport quantity, whereas its spin can only be assumed to remain fixed within the so-called spin flip length  $\lambda_{sf}$  [19].

## 2.2 Spin-dependent transverse velocity

In the previous section general definitions of spin and charge currents were given. However, it would be a mistake to view these two types of currents as independent of each other, as they are interconnected and can even be transformed into one another via spin-orbit interaction. This section will explain the origin and effect of spin-orbit interaction and thereafter elucidate the microscopic mechanisms that can create a velocity of the electrons that is transverse to their initial movement direction and dependent on their spin orientation.

### 2.2.1 Spin-orbit interaction (SOI)

The spin-orbit interaction describes the interaction of a particle's motion with its spin. In a semiclassical model, one uses the classical Bohr atomic model and assumes the reference frame of an electron. Within this reference frame the nucleus with the charge  $Ze$  moves around the electron. The circular movement of the nucleus charges creates a magnetic field  $\mathbf{B}_{\text{orb}}$  at the position of the electron that interacts with its spin-momentum  $\boldsymbol{\mu}_s$ . The energetic contribution of this interaction can be written as [14, 20]:

$$E_{so} = -\boldsymbol{\mu}_s \cdot \mathbf{B}_{\text{orb}} = \frac{a}{\hbar^2} \mathbf{s} \cdot \mathbf{l} \quad (2.3)$$

In this case  $\mathbf{s}$  is the spin-momentum of the electron,  $\mathbf{l}$  the angular momentum caused by the circular motion of the nucleus and  $a$  is equal to the spin-orbit coupling constant. The latter is proportional to the fourth power of  $Z$ . Therefore spin-orbit interaction plays a much bigger role in heavy atoms with a high value of  $Z$ , than in light ones.



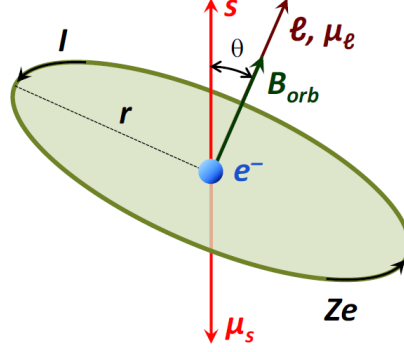


**Figure 2.2:** Semiclassical model of the spin-orbit interaction. In the reference frame of the electron, the circular movement of the atomic core creates a magnetic field  $\mathbf{B}_{orb} \parallel \mathbf{l}$  which interacts with the spin-momentum of the electron  $\boldsymbol{\mu}_s \parallel -\mathbf{s}$ . Taken from [14].

As one can see in Eq. (2.3), a parallel alignment of  $\mathbf{s}$  and  $\mathbf{l}$  is energetically favoured assuming positive values of  $a$ , so the electron spins align parallel to  $\mathbf{l}$ . In real solid states, this orbital momentum is mostly given by a certain crystalline direction in a crystal field that results in the interaction of electrons with the ions on neighboring lattice sites.

In an electrical conductor this spin-orbit coupling now gives rise to spin-dependent scattering effects that result in a spin-dependent transverse velocity of the electrons, which can lead to a separation of spin up and spin down electrons and thus to a spin current. The mechanisms that are responsible for this effect can be divided into two categories: Extrinsic effects that take place during the scattering of electrons on impurities, grain boundaries et cetera and intrinsic effects that occur in between said scattering events [19]. In the following, the most important extrinsic and intrinsic effects will be described.

Said transverse velocity effects can be understood in terms of the conductivity  $\hat{\sigma}$  which is a measure of a material's ability to conduct an electric current. In the two-dimensional Hall-bar geometry applied in this thesis it can be described as [14, 21]:

$$\mathbf{J}_q = \hat{\sigma} \mathbf{E} = \begin{pmatrix} \sigma_{xx} & \sigma_{xy} \\ \sigma_{yx} & \sigma_{yy} \end{pmatrix} \cdot \mathbf{E} \quad (2.4)$$

The diagonal elements of the conductivity tensor originate from the longitudinal motion of the current and are therefore referred to as  $\sigma_{long}$ , whereas transverse effects such as spin-dependent transverse velocity can give rise to off-diagonal contributions to  $\hat{\sigma}$  that are called  $\sigma_{trans}$ .

The inverse of the conductivity is the resistivity which is a measure of how strongly a material opposes the flow of the electric current. Its contributions can be determined by inverting the conductivity matrix [14, 21]:

$$\rho_{xx} = \frac{\sigma_{xx}}{\sigma_{xx}^2 + \sigma_{xy}^2} \quad (2.5)$$

$$\rho_{xy} = \frac{-\sigma_{xy}}{\sigma_{xx}^2 + \sigma_{xy}^2} \quad (2.6)$$

In this thesis a coordinate system with a charge current  $\mathbf{J}_q \parallel \mathbf{x}$  is applied. This allows to write  $(\sigma_{long} = \sigma_{xx}) / (\rho_{long} = \rho_{xx})$  and  $(\sigma_{trans} = \sigma_{xy}) / (\rho_{trans} = \rho_{xy})$ .

### 2.2.2 Extrinsic effects

For the extrinsic effects one has to distinguish between spin skew scattering [Fig. 2.3(a)] [22] and side-jump scattering [Fig. 2.3(b)] [23].

#### 2.2.2.1 Spin skew scattering

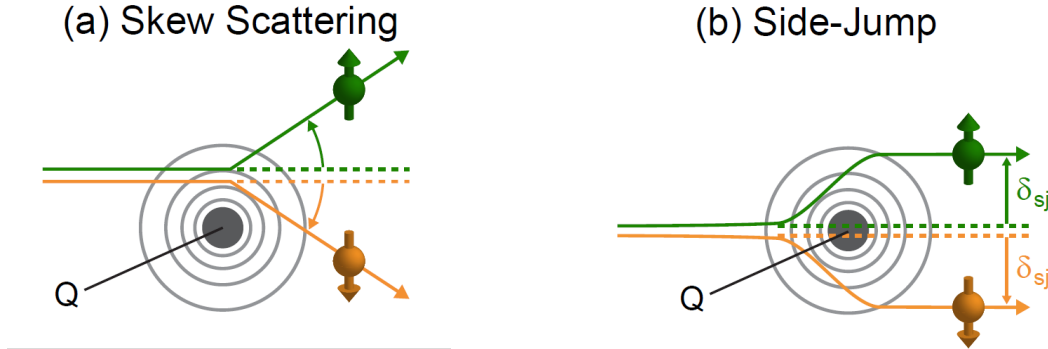


**Figure 2.3:** Illustration of the extrinsic spin-dependent transverse velocity effects. Skew scattering (a) is caused by the asymmetric scattering of electrons on an impurity due to spin-orbit interaction, whereas in side-jump scattering spin-orbit interaction causes a spin-dependent displacement due to acceleration and deceleration of electrons upon multiple scatterings. Taken from [18].

Skew scattering is the asymmetrical scattering of spin carrying particles on a central potential. As both the velocity of the electron and the scattering potential are space-dependent, the magnetic field acting on the electron is inhomogeneous. Due to spin-orbit interaction this creates an effective field gradient which, depending on the orientation of the spins, causes a force away or towards the scattering center [see Fig. 2.3(a)] [18, 22, 24]. In this way, the skew scattering causes a conductivity perpendicular to the movement of the electron which is independent of the impurity concentration, but dependent on the difference in spin-orbit coupling of the impurity and the conducting material as well as linearly proportional to the longitudinal conductivity  $\sigma_{\text{long}}$  [19].

#### 2.2.2.2 Side-jump scattering

Another extrinsic scattering mechanism is the so-called side-jump scattering caused by a spin-dependent acceleration and deceleration of electrons during the scattering. Multiple scattering events lead to an additional transverse displacement  $\delta_{sj}$  [see Fig. 2.3(b)] [23]. Apart from the case of high impurity concentrations, its contribution is negligible compared to spin skew scattering and intrinsic effects [25, 26]. In contrast to skew scattering, its conductivity contribution does not depend on  $\sigma_{\text{long}}$  [19].

### 2.2.3 Intrinsic effects

Intrinsic effects do not occur because of scattering events but due to the influence of the material-dependent bandstructure (see Fig. 2.4).

### 2.2.3.1 Bandstructure

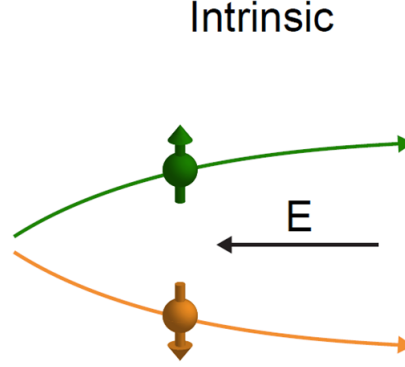


**Figure 2.4:** Illustration of the intrinsic spin-dependent transverse velocity effect. An external electric field gives rise to a velocity contribution perpendicular to the field direction and the Berry phase curvature  $\mathbf{\Omega}_k$ . Taken from [18].

In addition to impurity-dependent scattering mechanisms, the electronic band structure can also cause a spin-dependent transverse velocity effect, namely the so-called anomalous velocity that can be semiclassically described in terms of the Berry phase curvature  $\mathbf{\Omega}_k$  [27, 28].

$$\mathbf{v}_{k,\uparrow(\downarrow)} = \frac{1}{\hbar} \frac{\partial E_k}{\partial \mathbf{k}} \pm e\mathbf{E} \times \mathbf{\Omega}_k \quad (2.7)$$

Here the first term describes the classical velocity of Bloch wave electrons in a crystal lattice, whereas the second term creates a transverse velocity contribution perpendicular to the electric field  $\mathbf{E}$  [18]. This intrinsic contribution is independent of  $\sigma_{\text{long}}$  and is only dependent on the bandstructure itself [19].

### 2.2.4 Spin Hall effect (SHE) and its inverse (ISHE)

Now that the basic mechanisms that lead to spin-dependent transverse velocity effects have been explained, several interesting effects caused by it can be explored. First looking at a conventional charge current  $\mathbf{J}_q$  within a non-magnetic conductor with finite spin-orbit coupling, the mechanisms enlisted in the previous chapter cause a spin-dependent transverse velocity which leads to a separation of spin up and spin down electrons and thus to a spin current  $\mathbf{J}_s$ , that is perpendicular to both the spin of the electron and the charge current [see Fig. 2.5(a)]. This phenomenon is called the spin Hall effect (SHE)[8]. It can be described by the following formula [19]:

$$\mathbf{J}_s = \alpha_{SH} \left( -\frac{\hbar}{2e} \right) \mathbf{J}_q \times \mathbf{s} \quad (2.8)$$

The spin Hall angle  $\alpha_{SH}$  is a material-dependent constant that is a measure for the efficiency of the charge to spin-conversion. It can be written as  $\alpha_{SH} = \frac{\sigma_{SH}}{\sigma_{\text{long}}}$ . Here  $\sigma_{SH}$  is the spin Hall conductivity in contrast to the electrical conductivity  $\sigma_{\text{long}}$  [29].

Looking at the exact opposite case of a pure spin current, the spin up and spin down electrons are now deflected in the same directions due to their opposite direction of movement and spin. Therefore a pure charge current  $\mathbf{J}_q$  is created out of a pure spin current [see Fig. 2.5(b)]. This effect is the exact inverse of the previous case and is

called the inverse spin Hall effect (ISHE) [9]. It can be described as follows [19]:

$$\mathbf{J}_q = \alpha_{\text{SH}} \left( -\frac{2e}{\hbar} \right) \mathbf{J}_s \times \mathbf{s} \quad (2.9)$$

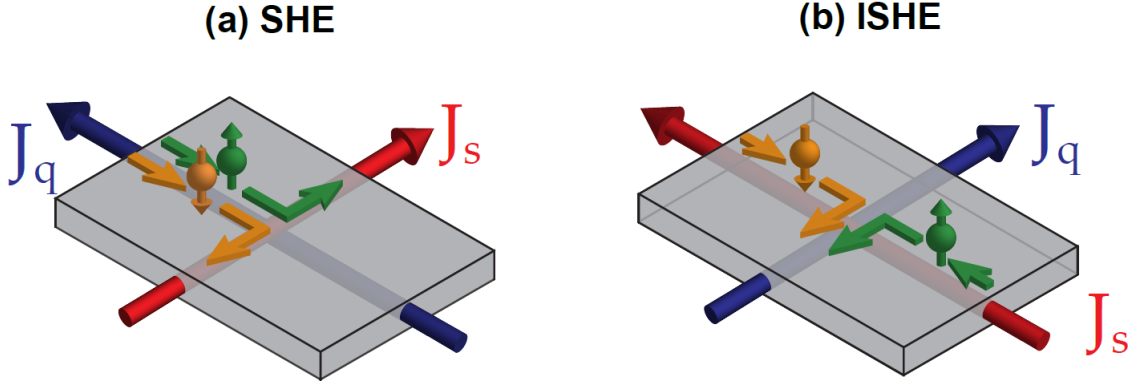


**Figure 2.5:** Manifestations of the transverse spin-dependent velocity mechanisms in paramagnetic conductors. In (a) The spin Hall Effect generates a spin current out of a charge current. Its inverse (b), the inverse spin Hall Effect generates a pure charge current out of a spin current. Taken from [18].

## 2.2.5 Anomalous Hall effect (AHE)

### 2.2.5.1 Definition of the AHE

The anomalous Hall Effect occurring in ferromagnetic conductors is caused by the same spin-orbit effects that are also responsible for the SHE and ISHE in paramagnets. However, the key difference between these phenomena is the unequal number of electrons aligned parallel to the magnetization  $\mathbf{M}$  of a ferromagnet to those orientated antiparallel. As depicted in Figure 2.6 for the ferromagnet nickel, this inequality is caused by the different density of states for spin up and spin down electrons at the Fermi energy [19].

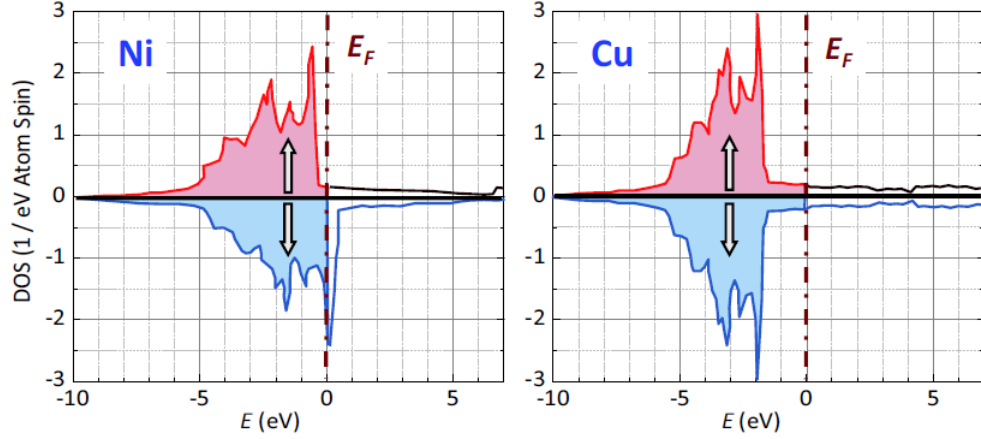


**Figure 2.6:** Density of states of the 3d and 4s states in the ferromagnetic nickel (left) as well as the paramagnetic copper (right). The 4s-electrons have a low density of states, ranging from -10 to 7 eV, whereas the 3d electrons have a high density of states that leads to a thin band. In the case of copper, there is no exchange interaction within the electrons, and thus both 3d $\uparrow$ - and 3d $\downarrow$ -bands are equally filled with electrons. In nickel, however, the exchange interactions of the electrons causes a shift of the 3d $\uparrow$  and 3d $\downarrow$ -bands of around 0.5 eV [14]. Therefore, a part of the 3d $\downarrow$ -states lie above the fermi energy level and remain unfilled, whereas the 3d $\uparrow$ -states are fully filled with electrons. Taken from [14].

Similarly to the paramagnetic case, a charge current in a ferromagnetic material again causes a perpendicular spin current. Due to the unequal number of spin up and spin down electrons, however, this also leads to a charge current in the transverse direction  $\mathbf{J}_{q,trans}$  (See Fig. 2.7). Since the spin orientation  $\mathbf{s}$  is parallel to the magnetization  $\mathbf{M}$ , the direction in which the transverse current is flowing is given by  $\mathbf{J}_q \times \mathbf{M}$  [19].<sup>3</sup>

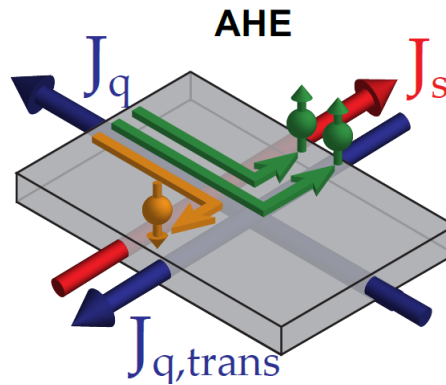


**Figure 2.7:** The anomalous Hall effect in ferromagnets causes a spin-polarized current perpendicular to the charge current due to spin-dependent scattering and an unequal number of spin up and spin down electrons. Taken from [18].

### 2.2.5.2 Behaviour of the AHE in an external magnetic field

This anomalous Hall effect was discovered in 1881 by Edwin H. Hall [10]. Two years before, he had made the groundbreaking discovery that the electrons of a current-carrying conductor in a magnetic field are "pressed to the side" by the Lorentz Force  $\mathbf{F}_L$  [30]. This transverse movement of the electrons causes a transverse voltage  $V_{trans}$

<sup>3</sup>Similar to the SHE, the efficiency of this conversion process is described by the anomalous Hall angle  $\alpha_{AHE} = \frac{\sigma_{AHE}}{\sigma_{long}}$ .

and thus a transverse electric field that is aligned so that it counteracts  $\mathbf{F}_L$  [31]. In a ferromagnetic conductor the behaviour of the transverse voltage greatly differs from the OHE, as can be seen in Fig. 2.8. Here, it is important to mention that the transverse resistivity  $\rho_{\text{trans}}$  on the y-axis is linearly proportional to the transverse voltage. More specific details about its quantity will be given in chapter 4. For low values of the external magnetic field  $\rho_{\text{trans}}$  changes up to two orders of magnitudes stronger than in paramagnetic materials. However, at larger values of  $H$  it saturates into a value that is nearly independent of the applied field. Its further increase at high values of  $H$  is due to the ordinary Hall effect [31]. Taking both the AHE and the OHE into account and restricting the geometry of the experiment to  $\mathbf{J}_q \parallel \mathbf{x}$ ,  $\mathbf{M} \parallel \mathbf{z}$ , such that the AHE only contributes to  $\rho_{\text{trans}}$ , it can be written as [19]:

$$\rho_{\text{trans}} = R_{\text{OHE}}\mu_0 H + R_{\text{AHE}}\mu_0 M = \rho_{\text{OHE}} + \rho_{\text{AHE}} \quad (2.10)$$

Here  $\mu_0$  is the vacuum permeability<sup>4</sup>.

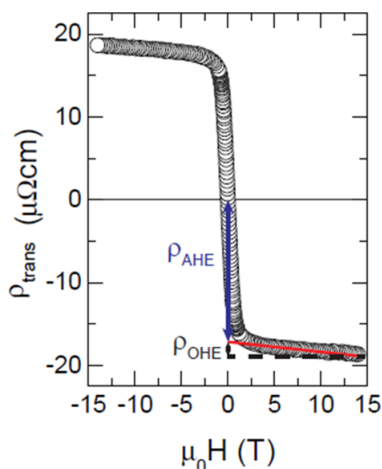


**Figure 2.8:** The transverse Hall effect behaviour of a 100 nm thin  $\text{Fe}_3\text{O}_4$  film measured at 200 K. The transverse resistivity  $\rho_{\text{trans}}$ , which is linearly proportional to the transverse voltage  $V_{\text{trans}}$ , changes very drastically for low values of the applied external field  $H_z$  due to the anomalous Hall effect, with increasing field strength, however, it saturates at a constant value. The remaining change of  $\rho_{\text{trans}}$  is due to the contribution of the ordinary Hall effect. Taken from [19].

### 2.2.5.3 Scaling behaviour of the AHE

As already discussed in sections 2.2.2 and 2.2.3, the microscopic phenomena responsible for the AHE scale differently with the longitudinal conductivity  $\sigma_{\text{long}}$ .

The most crucial question concerning the scaling behaviour of the AHE is, which of the three spin-dependent transverse velocity mechanisms is dominating for different material parameters, like conductivity, spin-orbit coupling strength et cetera. In past experiments, the behaviour of the transverse conductivity  $\sigma_{\text{AHE}}$  due to the anomalous Hall effect with respect to the longitudinal conductivity  $\sigma_{\text{long}}$  of the material has been investigated. Changing both the doping and temperature of the material,  $\sigma_{\text{long}}$  was varied over a large range of values for several different materials, and its relation to  $\sigma_{\text{AHE}}$  could be studied. By doing so, it was found that the dependence of  $\sigma_{\text{AHE}}$  on  $\sigma_{\text{long}}$  can be divided into three different regimes [19, 31, 32] as depicted in Fig. 2.9:

<sup>4</sup> $\mu_0 = 1.2566370614 \text{Vs}/(\text{Am})$

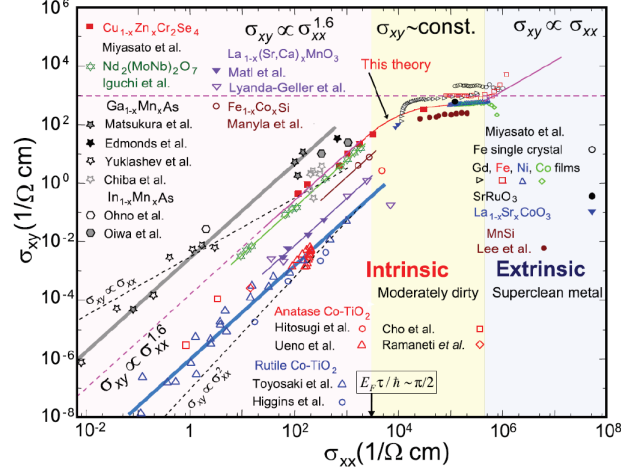


**Figure 2.9:** Behaviour of the transverse conductivity due to the anomalous Hall effect  $\sigma_{AHE}$  in several ferromagnetic conductors as a function of  $\sigma_{long}$ . Dependent on the magnitude of the latter, the plot can be divided into three scaling regimes: Bad-metal-hopping regime for  $\sigma_{long} < 10^4(\Omega\text{cm})^{-1}$ , Good-metal regime for  $10^4(\Omega\text{cm})^{-1} \leq \sigma_{long} \leq 10^6(\Omega\text{cm})^{-1}$  and High conductivity regime for  $\sigma_{long} > 1 \cdot 10^6(\Omega\text{cm})^{-1}$ . Taken from [32].

Very pure materials with a high conductivity  $\sigma_{long} > 1 \cdot 10^6(\Omega\text{cm})^{-1}$  are dominated by the skew scattering contribution. In this **high conductivity regime**, both conductivities are linearly proportional to one another  $\sigma_{AHE} \sim \sigma_{long}^1$ . The range from  $10^4(\Omega\text{cm})^{-1} \leq \sigma_{long} \leq 10^6(\Omega\text{cm})^{-1}$  is called the **good-metal regime**. In this area,  $\sigma_{AHE}$  is insensitive to changes in the longitudinal resistivity  $\sigma_{AHE} \sim \sigma_{long}^0 = \text{const.}$  Theoretically, it is assumed that this indicates that intrinsic mechanisms are the dominant contribution, while scattering mechanisms only play a secondary role. Lastly, in the **bad-metal-hopping regime**  $\sigma_{long} < 10^4(\Omega\text{cm})^{-1}$ , the conductivity due to the anomalous Hall Effect decreases with decreasing values of  $\sigma_{long}$ , with  $\sigma_{AHE} \sim \sigma_{long}^{1.6-1.8}$  which is currently not fully theoretically understood [19, 31].

## 2.3 Angle dependent magnetoresistance (ADMR) effects

Now that the interplay effects of spin and charge currents have been described, one can take a look at possible ways to detect and measure them. One important possibility is the application of angle-dependent changes of the magnetoresistance of ferromagnets and paramagnets that can result in the interaction of spin and charge currents. In the following, these effects will be named and explained.

### 2.3.1 Spin Hall magnetoresistance (SMR)

Spin currents can give rise to the spin Hall magnetoresistance (SMR) at the interface of a nonmagnetic conductor (NM) and a ferromagnetic insulator (FMI). As previously mentioned, a charge current through a paramagnetic conducting material can give rise to a spin current via the SHE, which causes a spin accumulation of spin up and spin down electrons on opposite sides of the nonmagnetic layer. Due to an imbalance in the spin resolved electrochemical potential  $\mu_s = \mu_{\uparrow} - \mu_{\downarrow}$ , this creates a **diffusive** spin current  $\mathbf{J}_s^{\text{diff}}$  that counteracts the initial spin current  $\mathbf{J}_s^{\text{SHE}}$  [33].

$$\mathbf{J}_s^{\text{diff}} = \frac{\hbar\sigma}{2c^2} \nabla \mu_s \quad (2.11)$$

In equilibrium, its contribution entirely balances  $\mathbf{J}_s^{\text{SHE}}$ :

$$\mathbf{J}_s^{\text{diff}} = -\mathbf{J}_s^{\text{SHE}} \quad (2.12)$$

In the steady state, the spin current  $\mathbf{J}_s$  created by the SHE has no influence on the initial charge current  $\mathbf{J}_q$ .

When bringing the nonmagnetic conductor (NM) into contact with a ferromagnetic insulator (FMI), however, this is not the case (see Fig. 2.10). The spin accumulations at the NM/FMI interface can now enter the ferromagnetic layer as a pure spin current  $\mathbf{J}_s^{\text{STT}}$ , which reduces  $\mathbf{J}_s^{\text{diff}}$  and thereby the cancellation of the SHE-generated spin current is no longer valid. This absorption of the spin accumulation in the FMI-layer occurs due to a spin transfer torque (STT) acting on its magnetic moments. It is proportional to  $\mathbf{M} \times \mathbf{s}$ , which makes it dependent on the angle between spin and magnetization. A detailed explanation of the origin and nature of said spin-transfer torque can be found in [34]. With this knowledge two limiting cases can be considered: For  $\mathbf{M} \parallel \mathbf{s}$  [see Fig. 2.10(a)], the spin transfer torque vanishes and no spin current can enter the FMI so that the resistivity of the NM remains unchanged. If  $\mathbf{M} \perp \mathbf{s}$  [see Fig. 2.10(b)], however, the spin accumulations are partly absorbed in the FMI and the unbalance between  $\mathbf{J}_s$  and  $\mathbf{J}_s^{\text{diff}}$  leads to a remaining transverse spin current, which has a finite diffusion length and contributes to the longitudinal resistivity  $\rho_{\text{long}}$  [19, 34]. This angle-dependent change in resistivity is called the spin Hall magnetoresistance SMR and can be described by the following formula [35, 36]:

$$\rho_{\text{long}} = \rho_0 + \rho_1 \cdot (1 - m_t^2) \quad (2.13)$$

$$\rho_{\text{trans}} = \rho_1 m_j m_t + \rho_2 m_n \quad (2.14)$$

In this case,  $m_t$ ,  $m_j$  and  $m_n$  are the projections of the magnetization direction onto  $\mathbf{t}$ ,  $\mathbf{j}$  and  $\mathbf{n}$ . Furthermore the  $\rho_i$  are the resistivity parameters.



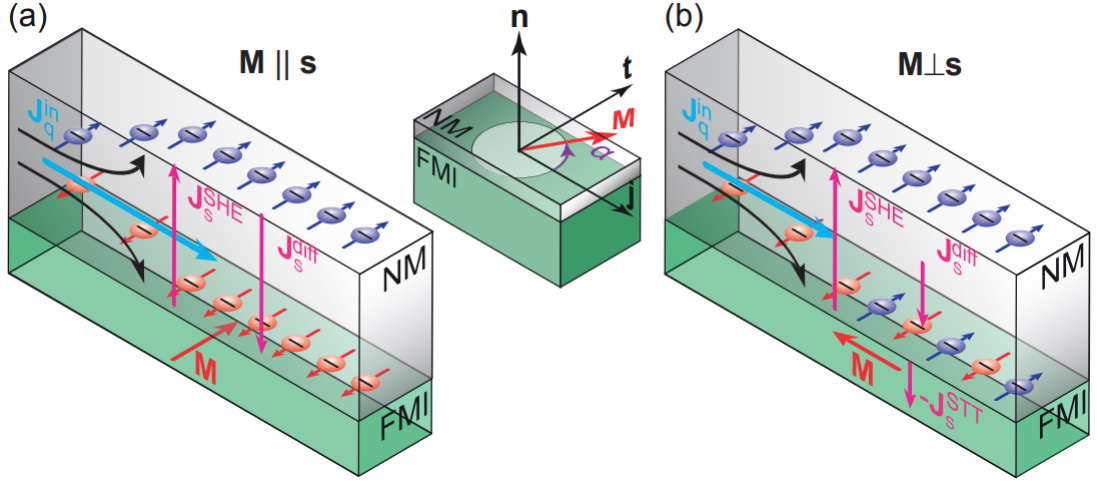


**Figure 2.10:** Illustration of the SMR-effect in a NM-FMI-interface. An initial charge current  $J_q$  gives rise to a spin current  $J_s^{\text{SHE}}$  via SHE which is counteracted by a diffusive spin current  $J_s^{\text{diff}}$ . Due to a spin transfer torque proportional to  $\mathbf{M} \times \mathbf{s}$  the spin accumulations can partly enter the ferromagnetic layer dependent on the angle between  $\mathbf{M}$  and  $\mathbf{s}$ . For the magnetization  $\mathbf{M} \parallel \mathbf{s}$  (a) no spin current can enter the FMI. The resistivity remains unchanged compared to the case of a current through a NM. For  $\mathbf{M} \perp \mathbf{s}$  (b) a part of the spin current  $J_s^{\text{STT}}$  can enter the ferromagnetic layer. This causes a reduction of  $J_s^{\text{diff}}$  and thereby it no longer fully counteracts  $J_s$  which leads to a remaining spin current in the NM-layer that increases its longitudinal resistivity. Taken from [33].

### 2.3.2 Angle-dependent contribution of the AHE

The anomalous Hall effect in a ferromagnetic conductor (FM) can also give rise to an angle-dependent change in the resistivity, as it generates a spin-polarized charge current perpendicular to both the magnetization of the ferromagnet  $\mathbf{M}$  and the charge current  $\mathbf{J}_q$ . Just like in the case of the SMR this causes an accumulation of spins on opposite sides of the conductor and via the spin chemical potential  $\mu_s$  a **diffusive** spin current  $J_s^{\text{diff}}$  is generated that counteracts the initial spin current  $J_s$ . The main difference to the case of the SMR is the unequal number of spin up and spin down electrons that lead to a transverse charge current  $\mathbf{J}_q$  and thus also to a transverse voltage  $V_{\text{trans}}$ . Furthermore, while the spins in a NM are geometrically fixed, their alignment is dictated by the orientation of  $\mathbf{M}$  in a FM due to dephasing of any transverse spin with respect to  $\mathbf{M}$  [37, 38]. As the spin accumulations caused by the AHE will always occur perpendicularly to both  $\mathbf{M}$  and  $\mathbf{J}_q$ , different orientations of the external magnetic field will lead to these accumulations developing on different sides of the conductor, as shown in Fig. 2.11.

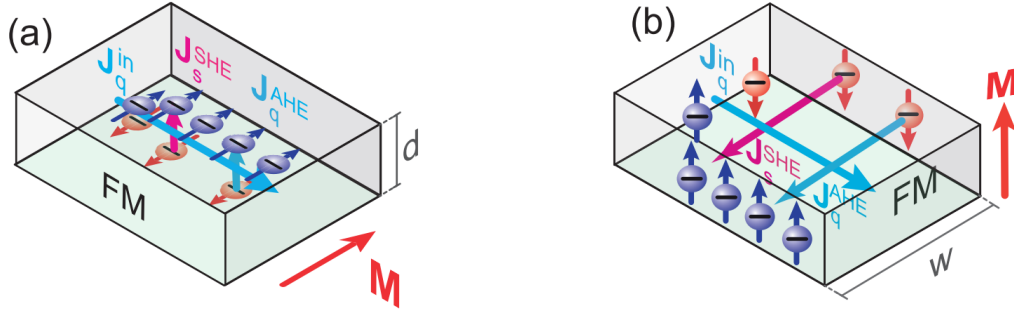


**Figure 2.11:** Depiction of the angle-dependent resistivity contribution of the AHE. In (a) the AHE causes an accumulation of spins with the ones being aligned parallel to the magnetization gathered on the upper side and the antiparallel ones on the bottom of the ferromagnetic conductor. In (b) the majority spins are positioned on the left side and the minority spins on the right side of the ferromagnet. Therefore, when rotating the FM in an external magnetic field, the spin accumulations switch between these two orientations and therefore contribute to  $\rho_{\text{long}}$  differently for different orientations of  $\mathbf{M}$ .

Dependent on the dimensions and shape of the FM, this leads to a change in transverse voltage and therefore to a change in resistivity of the FM [37]. A detailed mathematical derivation of this change can be found in [37], however, within this thesis just the final result of these calculations will be shown. The longitudinal change in resistivity within a ferromagnet due to an external magnetic field can be written as:

$$\frac{\rho_{\text{long}}}{\rho} = 1 - \left( \frac{\sigma_{\text{AHE}}}{\sigma} m_t \right)^2 - \frac{2\lambda_{\text{sf}}}{(1 - \beta^2)t} \left[ \frac{(\beta - \zeta)\sigma_{\text{AHE}}}{\sigma} \right]^2 m_t^2 \tanh \left( \frac{t}{2\lambda_{\text{sf}}} \right) \quad (2.15)$$

In this case  $m_t$  is the amplitude of the contribution of the magnetization that is transverse to the charge current, while  $\lambda_{\text{sf}}$  is the spin-diffusion length and  $t$  is the distance between the spin-accumulations due to the geometry of the sample. Additionally,  $\beta$  and  $\zeta$  are the spin polarizations of the currents caused by the AHE and AMR. The constant  $\frac{(\beta - \zeta)\sigma_{\text{AHE}}}{\sigma}$  can be viewed as a measure of the spin transfer torque efficiency due to the AHE. Applying arbitrary values for some of these constants, an exemplary plot of Eq. (2.15) as a function of the distance  $d$  is depicted in Fig. 2.12.

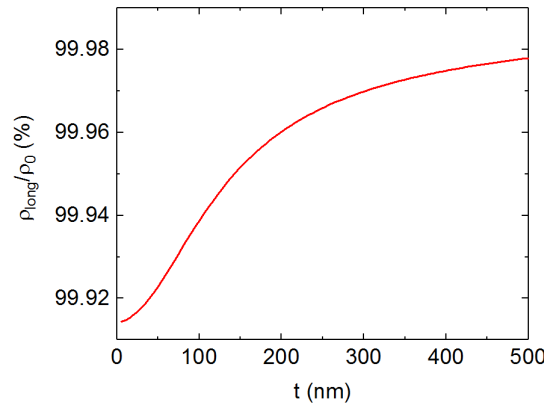


**Figure 2.12:** The normalized longitudinal resistivity as a function of the distance  $d$  between the spin accumulations. The values of  $|m_t| = 1$ ,  $\beta = -0.6$ ,  $\zeta = 1.6$  were chosen. According to its scaling behaviour in Fig. 2.9, the maximum value of  $\frac{\sigma_{\text{AHE}}}{\sigma} = 0.01$  for cobalt was selected and its spin diffusion length was estimated to be  $\lambda_{\text{sf}} = 40$  nm according to [37].

In Fig. 2.12 it becomes clear that the change in resistivity is the largest for small

distances between the spin accumulations, while saturating at a smaller constant value for larger  $t$ .

As in this thesis magnetic films with a very low layer thickness  $d$  were fabricated, these angle-dependent changes due to the AHE should be the most present when the AHE creates spin-accumulations on the top and bottom of the samples.

### 2.3.3 Anisotropic magnetoresistance (AMR)

In ferromagnetic conductors another magnetoresistance effect can be observed. Here, the resistivity for a charge current  $\mathbf{J}_q$  in parallel to the magnetization differs by several percent to that of one with  $\mathbf{J}_q \perp \mathbf{M}$ . This behaviour is depicted in Fig. 2.13 in dependence of an external magnetic field  $\mathbf{H}_{\text{ext}}$ . The difference between  $\rho_{\parallel}$  and  $\rho_{\perp}$  increases with increasing field strength up to a saturation value  $\mathbf{H}_s$  at which all elementary magnetic moments of the ferromagnet are aligned parallel to  $\mathbf{H}_{\text{ext}}$ . Upon further increase of the external field, both resistivities increase equally [39].

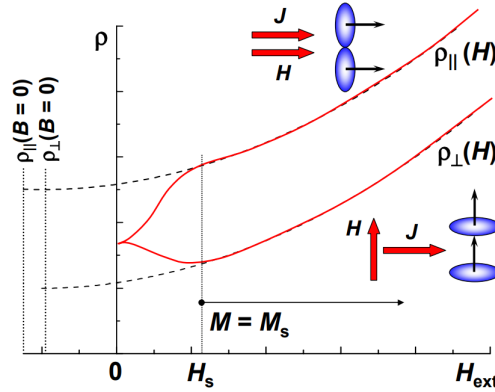


**Figure 2.13:** Common magnetic field dependence of the resistivity of a ferromagnetic conductor. The difference in resistivity between the cases of  $\rho_{\parallel}$  and  $\rho_{\perp}$  increases with  $\mathbf{H}_{\text{ext}}$ , due to magnetic domain shifts within ferromagnets that need to take place, before the atomic magnetic moments can all align according to the external field. In order to get the real values of  $\rho_{\parallel}$  and  $\rho_{\perp}$ , one has to extrapolate their behaviour above  $\mathbf{H}_s$  for  $B=0$  T. Furthermore, an aspherical distribution of electrons in an external magnetic field due to spin-orbit interactions in both cases is depicted. Taken from [39].

The physical origin of the AMR lies once again in spin-orbit interaction, which causes an aspherical charge distribution within the ferromagnetic layer. Also due to SOI its alignment is dependent on the orientation of the magnetic moments controlled by the external magnetic field  $\mathbf{H}_{\text{ext}}$ . Due to its aspherical shape, the scattering cross section of the charge distribution varies with the alignment of  $\mathbf{M}$ . Therefore, for different orientations of the magnetization, the magnitude at which the conducting electrons are scattered within the ferromagnetic layer and hence its resistivity changes (see Fig. 2.14) [39, 40].

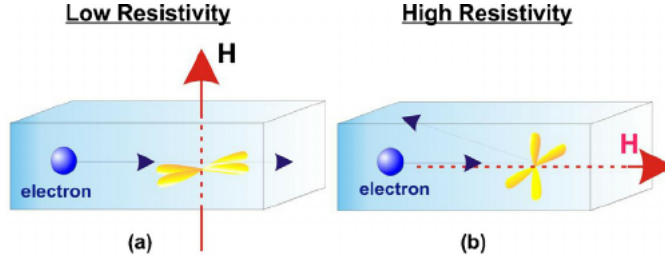


**Figure 2.14:** Schematic representation of the origin of the AMR. Due to spin-orbit interaction, the aspherical distribution of charge carriers is coupled to the alignment of the magnetic moments. Subsequently, electrons are scattered differently strong for varying orientations of the external magnetic field  $\mathbf{H}$ . In (a),  $\mathbf{H} \perp \mathbf{J}_q$ , and hence the charge distribution is aligned, so that its scattering cross section for incoming electrons is very low, which results in a lower resistivity value of  $\rho_{\perp}$ . In (b), however,  $\mathbf{H} \parallel \mathbf{J}_q$ , so that the scattering cross section is larger and more electrons are scattered, which results in a higher value of  $\rho_{\parallel}$ . Taken from [41].

Similarly to the case of the SMR-effect, the change in resistivity due to the AMR-effect can be expressed as [13, 42]:

$$\rho_{long} = \rho_0 + \rho_1 \cdot m_j^2 \quad (2.16)$$

$$\rho_{trans} = \rho_1 m_j m_t + \rho_2 m_n \quad (2.17)$$

Here again  $\rho_i$  represent the resistivity parameters and the magnetization projections onto  $\mathbf{t}$ ,  $\mathbf{j}$  and  $\mathbf{n}$  are given by  $m_t$ ,  $m_j$  and  $m_n$ .

# Chapter 3

## Experimental techniques

This chapter gives insight into the fabrication of thin film ferromagnetic samples and the microstructuring process for electronic transport measurements. This is followed by a description of the general measurement process of ADMR-experiments in the "Moria"-cryostat.

### 3.1 Sample fabrication

#### 3.1.1 Work at the ultra-high Vacuum (UHV) Cluster

In a first step, two Hall-bar structures are patterned perpendicularly to each other on a plain Si-chip via photolithography<sup>1</sup> into a resist layer. Afterwards, the sample is inserted into the UHV Cluster, where a layer of cobalt with varying thickness is deposited in the Hall-bar structures via electron-beam evaporation (EVAP).<sup>2</sup> Finally in the sputtering chamber, a thin layer of aluminium is sputtered on top in order to prevent the Co from reacting with the oxygen in the air.<sup>3</sup> Due to its low value of  $Z$ , the Al-layer should not cause a significant SMR-effect. Afterwards, the coating with the unnecessary material and the resist layer are carefully removed by placing the substrate in acetone p.a. and isopropanol p.a. in an ultrasonic bath.

---

<sup>1</sup>After having been cleaned with acetone p.a. and isopropanol p.a., the sample is covered in AZ5214E-fotoreist-coating and placed on a hotplate at 110°C for 70 seconds. The Hall-bar pattern is generated by exposing the coating to the light of a mercury vapour lamp for 42 seconds and developed in AZ 726 MIF developer for around 20 seconds [42].

<sup>2</sup> A crucible containing cobalt is heated by a highly energetic electron beam with an accelerating voltage of -7.5 kV until it is vaporized. An oscillating crystal is used to determine the deposition rate. In this case a constant rate of 1.0 Å/s is applied and the beam current is adjusted to maintain this constant rate. Furthermore, a shutter is used to automatically screen the sample until the required rate is achieved and after the given thickness is reached.

<sup>3</sup> During the sputtering process, the solid target material Al is bombarded with ionized Ar-ions and thereby Al particles are ejected into the gas phase. If a substrate is placed close to the target, they can condensate on top of it and form a thin layer. During the sputtering process, a constant pressure of  $4.0 \cdot 10^{-3}$  mbar is maintained. After two minutes of pre-sputtering, the shutter is opened for about 30 seconds to deposit approximately 2-3 nm of aluminium.

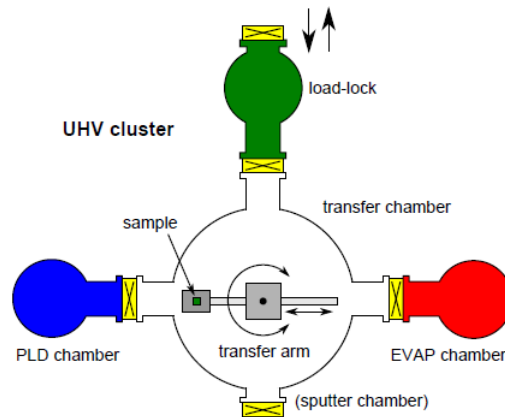


**Figure 3.1:** Schematic representation of the UHV Cluster. The sample is inserted through the load-lock at room pressure. Then the load-lock is getting pumped out by a turbo pump. Once the pressure drops below  $3.0 \cdot 10^{-7}$  mbar, the transfer arm can be used to transport the sample into the different deposition chambers. The sample is placed in the EVAP-chamber to deposit a layer of Co with varying thickness values and afterwards into the sputtering chamber in order to sputter a thin layer of Al on top of the sample to protect the cobalt from reacting with oxygen. Taken from [43].

### 3.1.2 Final steps

Again, via means of optical lithography, the contact areas of the Hall-bar are patterned and a layer of gold with a thickness of approximately 40 nm is deposited using the small sputtering device.<sup>4</sup> The advantage of gold on the pads of the Hall-bar is explained below. Afterwards another liftoff-process is implemented to remove the resist. The finished sample is glued with GE-varnish<sup>5</sup> on a block of copper which itself is connected to a chip carrier. The sample contact areas are connected to the pads of the chip carrier with aluminium wires via wedge bonding [42]. Here, the presence of gold leads to a better visibility of the pads as well as an improved bond adhesion. The standard bonding scheme applied in this thesis can be found in the Appendix in Fig. A.1. An illustration of a finished sample is shown in Fig. 3.2. In the course of this thesis, 17 samples with a thickness ranging from 4-120 nm were fabricated and are listed in the appendix A.2. The thickness of some of these samples was investigated using X-ray diffraction (XRD) data.<sup>6</sup> It was found that the effective thickness was on average 10% smaller than its ideal value. Consequently within this thesis, all values of the layer thickness  $d$  have been multiplied by the factor 0.9.<sup>7</sup>

Due to a strange behaviour of the sample with a thickness of 27 nm, a second sample of the same thickness was fabricated. This also serves as a measure of the reproducibility of these kind of samples when comparing their results.

<sup>4</sup> The sputtering process here works analogously to above. The gold is sputtered at a constant pressure of  $5.0 \cdot 10^{-2}$  mbar and at a constant current of 45 mA. After 100 s of presputtering, the shutter is opened for 60 s, which should be roughly equivalent to a layer thickness of 40 nm.

<sup>5</sup> VGE-7031 varnish

<sup>6</sup> Within the applied X-ray machine of the type D8 Discover, monochromatic light is radiated on the sample with an angle  $\omega$  and detected at an angle  $2\theta$ . During the XRD-measurement a  $2\theta$ - $\omega$ -scan is conducted and the detected counts are plotted against the angle  $2\theta$ . To determine the real layer thickness, the program LEPTOS is applied to compare the received data to simulated results based on the assumed layer thickness. By varying parameters like roughness and Co/Al-layer thickness, the theory curve corresponding the best to the experimental results is found.

<sup>7</sup> When a sample is named in this thesis, the given value of  $d$  always refers to its effective thickness

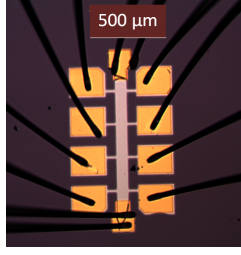


**Figure 3.2:** Microscope image of a finished sample. The black lines are the thin aluminium wires that connect the pads of the sample to those of the chip carrier.

## 3.2 Procedure of the ADMR measurement

### 3.2.1 The "Moria"-cryostat

All ADMR-measurements in this thesis are conducted with the "Moria"-cryostat (Magneto-Optical-Resistance-Investigation-Apparatus), where a superconducting split coil magnet is used to generate a constant magnetic field with a magnitude of up to  $\mu_0 H = 7$  T. The finished sample is mounted on a dipstick and placed in the variable temperature insert (VTI) in the center of the cryostat. The temperature within the VTI is controlled by a heater as well as by the flow of helium through a needle valve. The measurements in the moria-cryostat are controlled by DR4ever, a LabView based software [42].

The general measurement scheme of a sample within the cryostat is depicted in Fig. 3.3. An external magnetic field is applied, while a fixed charge current is driven through the main bridge of the Hall-bar with a Keithley 2400 Sourcemeater. While the sample is now rotated stepwise in an axis that is perpendicular to the magnetic field, the values of  $V_{long}$  and  $V_{trans}$  are measured after each step. The longitudinal changes of the voltage in both Hall-bars are recorded with Keithley K2182 Nanovoltmeters as they are more precise than the Keithley 2010 Multimeters used to measure  $V_{trans}$ . The standard Hall-bar pads used for these measurements are given in the appendix Tab. A.1.

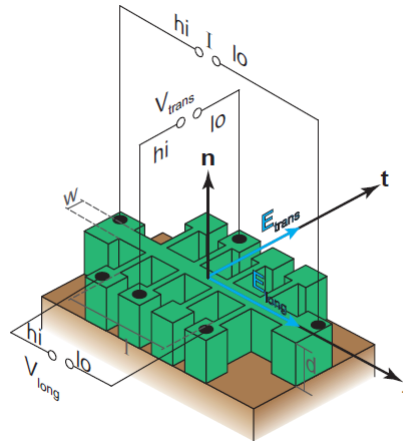


**Figure 3.3:** Illustration of the Hall-bar measurement geometry. Constant current is driven through the trunk of the Hall-bar. While the sample is rotated in a plane perpendicularly to the direction of the external magnetic field, the changes of the longitudinal and transverse voltages are measured. Taken from [19].

The ADMR-measurements in this thesis are all conducted at 300 K, with a step-width

of  $10^\circ$  in the interval from  $-20^\circ$  to  $380^\circ$ . In order to detect the behaviour of  $\rho_{trans}$  of the ferromagnetic conductor in an external field (see Fig. 2.8) in both the ranges dominated by the AHE for  $H < H_s$  and the OHE for  $H > H_s$ , these measurements are conducted at five different field strengths ranging from 7 T to 0.5 T.

### 3.2.2 Definition of the different measurement geometries

In the coordinate system depicted in Fig. 3.3 with  $\mathbf{j} \parallel \mathbf{x}$ ,  $\mathbf{t} \parallel \mathbf{y}$  and  $\mathbf{n} \parallel \mathbf{z}$ , three different measurement geometries are possible. All of them are depicted in Fig. 3.4. In the in-plane (ip) geometry (a), the rotation axis is given by  $\mathbf{n}$  with the magnetic-field acting in the  $\mathbf{j}$ - $\mathbf{t}$ -plane. In this configuration the behaviour of  $V_{long}$  and  $V_{trans}$  should be equivalent apart from being phase-shifted  $45^\circ$ . In out-of-plane-orientation the magnetic field is initially parallel to  $\mathbf{n}$ , however, one has to distinguish between two cases depending on the rotation axis. In the oopj-orientation (b) it is given by  $\mathbf{j}$  with the unit magnetic field vector  $\mathbf{h} = \frac{\mathbf{H}}{|\mathbf{H}|}$  moving in the  $\mathbf{n}$ - $\mathbf{t}$ -plane, whereas in oopt-direction (c) the Hall-bar is rotated around  $\mathbf{t}$  in the  $\mathbf{j}$ - $\mathbf{n}$ -plane.

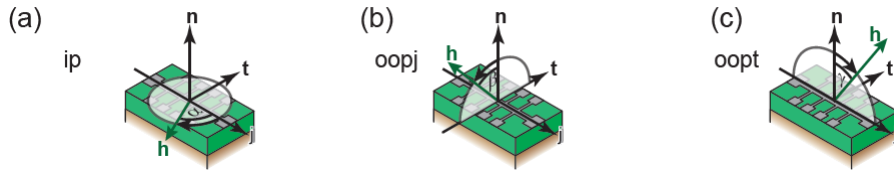


**Figure 3.4:** Illustration of the different Hall-bar measurement geometries. Taken from [19].

The dipstick offers two connections for both in-plane and out-of-plane-orientation (see Fig. 3.5). As shown in Fig. 3.5, in the latter both the oopj- and oopt-cases can be investigated during the same measurement as the upper vertical Hall-bar of the sample is orientated in oopj-geometry, while the orientation of the lower horizontal one is equal to the oopt-geometry.

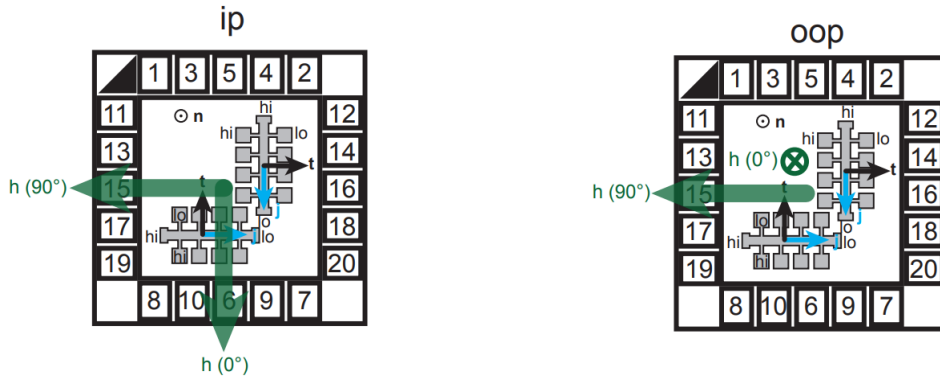


**Figure 3.5:** Illustration of the orientation of the external magnetic field with respect to the chip carrier system of the dipstick in the Moria Cryostat in ip- and oop-geometry. Taken from [44].



# Chapter 4

## Results and discussion

This chapter will illustrate the results of the conducted measurements. Firstly, a general overview on how to extract the individual effects out of the "raw" data is given. Afterwards, the measured size effect of the anisotropic magnetoresistance is illustrated in the ip as well as the oopj and oopt-orientation. Subsequently, the scaling behaviour of the AHE is investigated and compared to previous experimental results shown in section 2.2.5.3. Additionally, it is explored to what extent its angle-dependent contribution is visible in the results of the oopj-geometry. At last a first attempt at the Walther-Meißner-Institute to detect the USMR-effect in cobalt platin bilayers is described.

### 4.1 Finite size effects of the anisotropic magnetoresistance

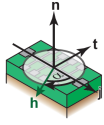
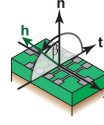
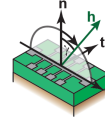
#### 4.1.1 Data evaluation

In order to determine the thickness-dependent resistivity out of the measured values of  $V_{\text{long}}$  and  $V_{\text{trans}}$ , one has to take into account the geometry of the Hall-bar structure. With its width  $w = 80 \mu\text{m}$  and a longitudinal distance between two neighboring measuring probes of  $l = 200 \mu\text{m}$  as well as the magnitude of the applied charge current  $I$ ,  $\rho_{\text{long}}$  and  $\rho_{\text{trans}}$  can be calculated by the following formulae.

$$\rho_{\text{long}} = \left( \frac{V_{\text{long}}}{I} \right) \frac{w \cdot d}{l} \quad (4.1)$$

$$\rho_{\text{trans}} = \left( \frac{V_{\text{trans}}}{I} \right) d \quad (4.2)$$

Before the experimental angle-dependent changes of the resistivity are investigated, firstly a quick look is taken at the theoretically expected behaviour of  $\rho_{\text{long}}$  and  $\rho_{\text{trans}}$ . As mentioned previously in section 2.3.3, the change in longitudinal resistivity due to the AMR scales with  $m_j^2$ . Assuming  $\mathbf{h} \parallel \mathbf{m}$  for all magnetic field orientations, the magnetization vector in the three different geometries can be expressed as:

ip	oopj	oopt
		
$\mathbf{m} = \begin{pmatrix} \cos \alpha \\ -\sin \alpha \\ 0 \end{pmatrix}$	$\mathbf{m} = \begin{pmatrix} 0 \\ -\sin \beta \\ \cos \beta \end{pmatrix}$	$\mathbf{m} = \begin{pmatrix} \sin \gamma \\ 0 \\ \cos \gamma \end{pmatrix}$

**Table 4.1:** Mathematical expression of the magnetization vector in the three different measurement geometries assuming  $\mathbf{h} \parallel \mathbf{m}$ . Images taken from [19].

Applying these  $\mathbf{m}$  in Eq. (2.16), one would expect an in-plane behaviour of  $\cos^2 \alpha$ , a  $\sin^2 \gamma$ -behaviour of the same amplitude  $\rho_1$  in oopt-geometry and no changes of  $\rho_{\text{long}}$  in oopj as illustrated in Fig. 4.1.

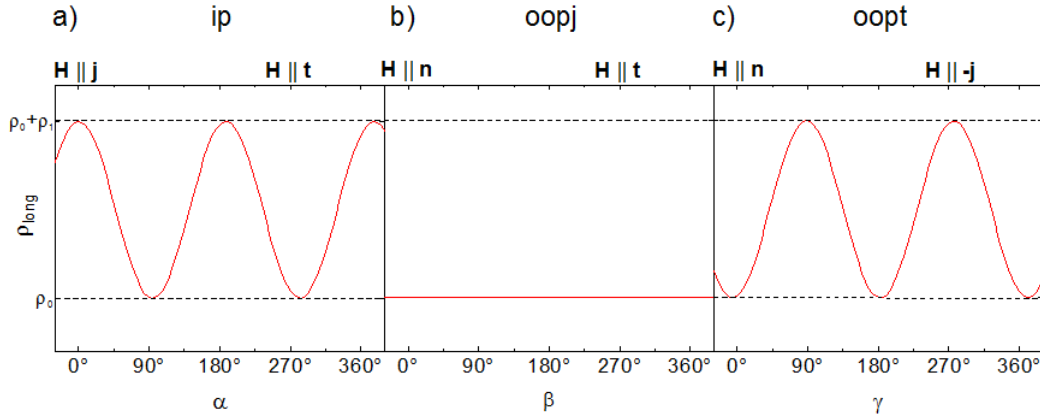


**Figure 4.1:** Expected behaviour of  $\rho_{\text{long}}$  due to the AMR for  $\rho_1 > 0$  in the three possible measurement geometries. In the ip-geometry (a), a  $\cos^2 \alpha$  dependence is expected, while in the oopt-case (c) a  $\sin^2 \gamma$  of the same amplitude should occur. In oopj-geometry (b) the AMR does not give rise to any changes in resistivity.

The transverse resistivity-dependence of the AMR is given in Eq. (2.17). In ip-orientation  $m_n = 0$  and the remaining contribution is proportional to  $-\cos \alpha \sin \alpha$  and, as mentioned beforehand, of the same amplitude as in the longitudinal case. In oopj and oopt either one of  $m_j$  and  $m_t$  vanishes, leaving only the  $\cos \beta / \gamma$ -contribution of  $m_n$ . The resulting theoretical angle-dependent behaviour of  $\rho_{\text{trans}}$  is depicted in Fig. 4.2. Here a negative value of  $\rho_2$  is assumed.

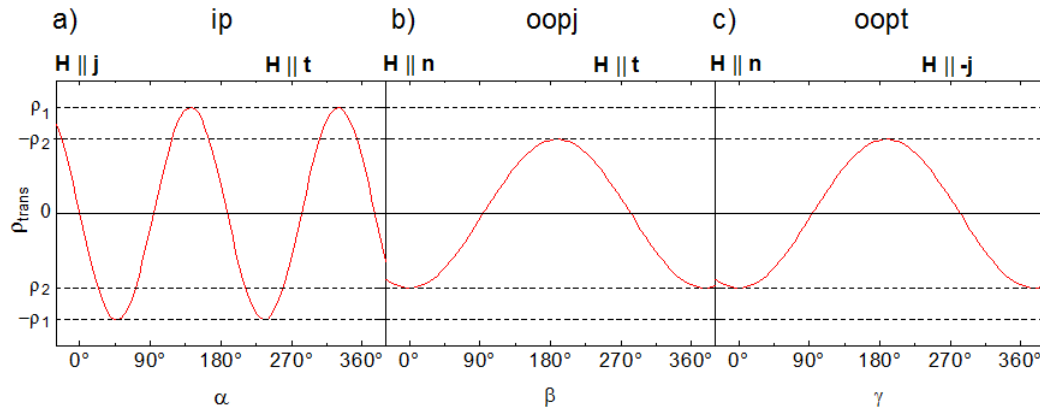


**Figure 4.2:** Expected behaviour of  $\rho_{\text{trans}}$  for  $\rho_1 > 0$ ,  $\rho_2 < 0$  due to the AMR in the three possible measurement geometries. In the ip-geometry (a), a  $\cos \alpha \sin \alpha$  dependence is expected, while in both the oopj-case (b) and in the oopt-case (c) a  $\cos \beta / \gamma$ -behaviour should occur.

The theoretical longitudinal ADMR-pattern in Fig. 4.1 can now be compared to the one that is actually being measured depicted in Fig. 4.3.

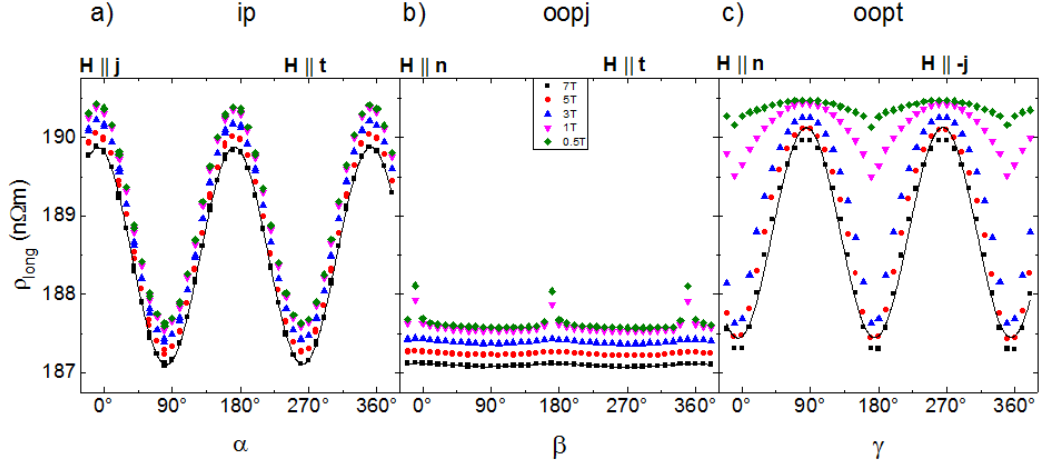


**Figure 4.3:** Measured longitudinal ADMR behaviour of the resistivity in a 45 nm thick layer of cobalt in each of the three possible measurement geometries for 5 different amplitudes of the magnetic field from 7 T to 0.5 T.

As one can see in Fig. 4.3, the measured ADMR-behaviour of the cobalt thin films corresponds quite nicely to theory with the ip and oopt-data showing the expected  $\cos^2 \alpha$  and  $\sin^2 \gamma$  behaviour with a small phase shift due to an imperfect sample alignment. For the larger values of the magnetic field their amplitudes are in good agreement, while in the oopt-geometry for lower values of  $H$  the magnetic moments can no longer fully align in parallel to the external magnetic field, due to magnetic anisotropy, which results in a decrease of the  $\rho_1$ -amplitude. Generally, in all geometries it is apparent that the longitudinal resistivity shows a dependence on  $H$ . This is due to "pinning" effects on the surface of the ferromagnetic conductor where the magnetic moments of the ferromagnet have a preferred orientation to minimize the magnetic stray field. With rising levels of the magnetic field, however, more and more of them are forced to align in parallel to the magnetic field, which results in a field-dependent change of the resistivity. Another possible origin for the field-dependence could be related to additional negative MR effects due to the bandstructure of Co.

Contrary to the expected indifference to the AMR, the oopj-geometry shows a  $\sin^2 \beta$ -conduct of  $\rho_{\text{long}}$  with a maximum value when  $\mathbf{H} \parallel \mathbf{n}$  and a minimum at  $\mathbf{H} \parallel \mathbf{t}$ . One possible explanation of this is a misalignment-dependent contribution of the AMR due to a tilt of the sample that cannot be glued perfectly orthogonally. However, an additional contribution might come from angle-dependent effects of the AHE discussed in section 2.3.2 where it has been assumed that its influence should be the most present for spin-accumulations occurring on top and bottom of the sample. This occurs when  $\mathbf{H} \parallel \mathbf{t}$  and would therefore be an explanation for the minimum value of  $\rho_{\text{long}}$  at this orientation. Generally, the results of the three geometries are slightly shifted against one another due to the fact that each of them have been detected in three different measurements with a possible slight difference in temperature.

In order to determine the AMR amplitude, these "raw"-data are fitted with a  $\sin^2$ -formula of the following type:

$$\rho_{\text{long}}(\theta) = \rho_0 + \rho_1 \cdot \sin^2 \left( \pi \frac{(\theta - \theta_c)}{w} \right) + k \cdot \theta \quad (4.3)$$

Here  $\theta_c$  represents the occurring phase shift,  $w$  determines the periodicity and is kept at

the fixed value of  $180^\circ$ . A possible linear temperature drift within the measurements is taken into account by the additional  $k \cdot \theta$ -contribution. Especially when dealing with the small amplitudes of the oopj-geometry, a temperature-driven change of the resistivity can alter the results. The MR amplitude for each rotation plane can now be calculated by the following equation:

$$\left( \frac{\Delta\rho}{\rho} \right)_{\text{long}} = \left| \frac{\rho_1}{\rho_0} \right| \quad (4.4)$$

Here  $\rho_0$  is the longitudinal resistivity of the ferromagnetic conductor.

Before discussing the results of this analysis we also look into the experimental results for the transverse resistivity shown in Fig. 4.4.

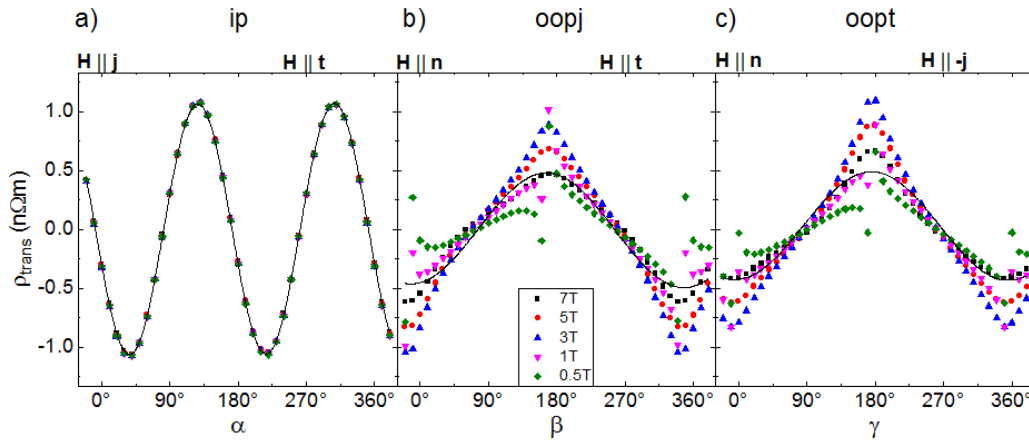


**Figure 4.4:** Measured transverse ADMR behaviour of the resistivity in a 45 nm thick layer of cobalt in each of the three possible measurement geometries for 5 different amplitudes of the magnetic field from 7 T to 0.5 T. The offset of  $\rho_{\text{trans}}$  has been corrected.

The experimental results are in quite good agreement with the theoretical assumptions. The transverse ip-behaviour can also be viewed as a shifted  $\sin^2 \alpha$ -function of an amplitude that is of approximately the same amplitude as in the longitudinal case, however, "pinning"-effects do not play a role in the transverse and consequently  $\rho_0$  is nearly  $H$ -independent.

As assumed, the oopj- and oopt-data show an almost identical behaviour apart from being slightly shifted against one another due to temperature differences between the two measurements. The apparent dependence of  $\rho_{\text{trans}}$  on the external magnetic field is caused by the transverse currents induced by the OHE in the range of  $H \geq 3$  T. Furthermore, for lower values of  $H$ , their magnetic moments remain in-plane due to magnetic anisotropy and their orientation can only tilt in out of plane direction to a small degree, which results in a lower amplitude. At  $180^\circ$ , however, the change of sign of  $H$  causes them to flip their orientation. This leads to an abrupt change in resistivity from the ip AMR that can be seen at Fig. 4.4 in the displacement of the oop-data points at  $180^\circ$ . Upon returning to the starting position at  $0^\circ/360^\circ$  the magnetization is flipped back again.

The ip-data can again be fitted with formula (4.3) while the oopj- and oopt-results

are described by a sin-function.

$$\rho_{\text{trans}}(\theta) = \rho_2 \cdot \sin\left(\pi \frac{(\theta - \theta_c)}{w}\right) + k \cdot \theta \quad (4.5)$$

Again a fixed periodicity of  $w = 180^\circ$  is assumed and the temperature drift is included by  $k \cdot \theta$ . In this case the AMR-amplitude is equal to:

$$\left(\frac{\Delta\rho}{\rho}\right)_{\text{trans}} = \left|\frac{\rho_2}{\rho_0}\right| \quad (4.6)$$

#### 4.1.2 Thickness-dependent behaviour of the resistivity

Before looking at the AMR-amplitudes in the three different geometries, the thickness-dependent behaviour of the longitudinal resistivity  $\rho_0$  is studied and compared to the theoretical predictions of the Fischer's Formula [45], which includes interface scattering contributions.

$$\rho_{\text{co}}(d_{\text{Co}}) = \rho_\infty \left(1 + \frac{3}{8(d_{\text{Co}} - h)} [l_\infty(1 - p)]\right) \quad (4.7)$$

Here  $\rho_\infty$  and  $l_\infty$  describe the resistivity and mean free path of an infinitely thick sample,  $h$  is a measure of the surface roughness contribution and usually takes material-dependent values in the range of (0.5-1.0)nm, while  $p=(0-1)$  takes the interface scattering into account. In Fig. 4.5 the measured longitudinal resistivities  $\rho_0$  of the samples are plotted against their layer thickness  $d_{\text{Co}}$ . By fitting the data to Eq. (4.7) with  $\rho_\infty$  and  $l_\infty$  as fit parameters in Origin, these experimental results can be compared to the theoretical behaviour of the Fischer formula with varying values of  $h$  and  $p$ . The result for the best-fitting function is depicted in Fig. 4.5 as a red line.

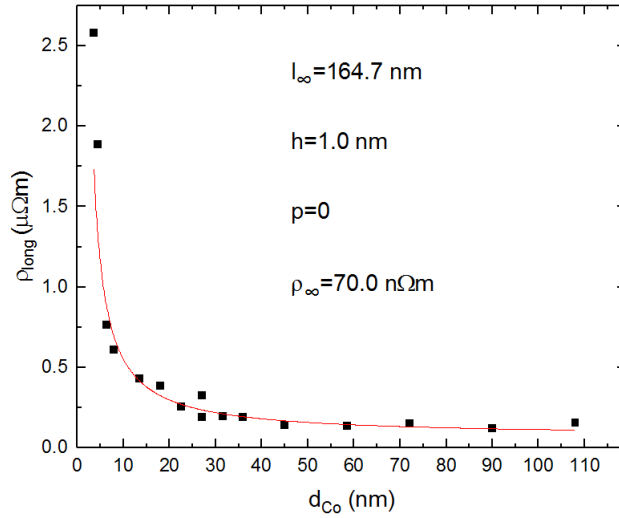


**Figure 4.5:** Measured mean value of the longitudinal resistivity of both Hall-bars as a function of the layer thickness. The data-points are fitted with a Fischer-type formula (Eq. (4.7)).

The best fitting function to describe the curvature of the data points when approaching the asymptotic limit was found for a high value of  $h = 1.0$  nm. As for low values of  $d_{\text{Co}}$  the right term in Eq. (4.7) is much larger than 1, the fit is nearly independent of the parameter  $p$  as Origin just adapts the value of  $l_\infty$  correspondingly such that  $p=0$  has been chosen.

Here a first example of the unusual behaviour of the first 27-nm-sample can be seen in its resistivity being situated a lot higher than that of both the theory curve as well as that of the second sample of the same thickness. According to the fit  $\rho_\infty = (70.0 \pm 14.8) \text{ n}\Omega\text{m}$  which is in good agreement to its literature value of  $58.0 \text{ n}\Omega\text{m}$  found in [46]. However, the value of  $l_\infty = (164.7 \pm 48.9) \text{ nm}$  does not correspond to its literature value of  $5.5 \text{ nm}$  [37]. Reasons for this difference are on the one hand the presence of the thin layer of Al sputtered on top of the Co-film and on the other hand potential variations of the thickness of the Co-layers on the sample. Additionally, the magnitude of  $l_\infty$  is mostly dictated by the behaviour of the thinner samples, where its contribution is the largest. In this range, additional resistivity effects caused, for example, by impurities are the most present and lead to a steep increase of  $\rho_{\text{Co}}$  for low  $d_{\text{Co}}$  and thus alter  $l_\infty$ .

### 4.1.3 In-plane-results

In the case of the in-plane measurements the mean value of both Hall-bars for the amplitude of the the longitudinal as well as the transverse AMR-effect  $\left(\frac{\Delta\rho}{\rho}\right)$  at  $\mu_0 H=7 \text{ T}$  was calculated. Its behaviour in dependence of the layer thickness  $d$  is depicted in Fig. 4.6.

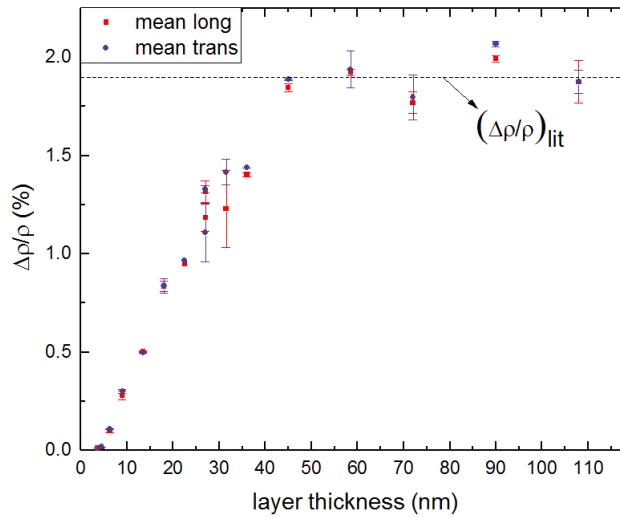
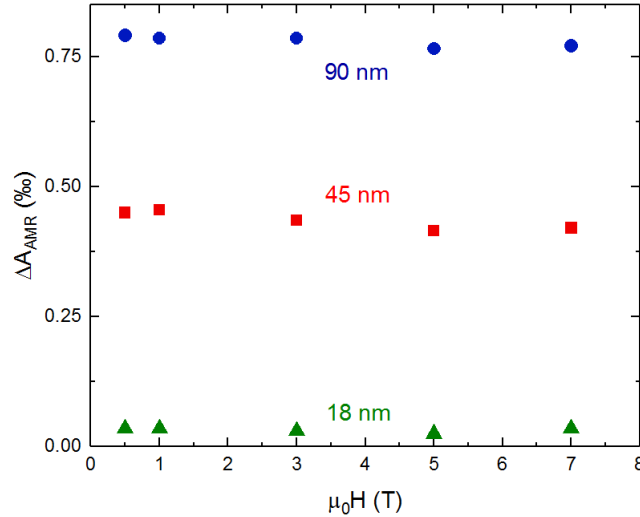


**Figure 4.6:** Dependence of the longitudinal and transverse AMR-amplitude in ip-geometry of the layer thickness for a magnetic field of 7 T. Here a mean value of its values in both of the investigated Hall-bars together with its standard deviation as error bars is plotted as well as the literature value of  $\left(\frac{\Delta\rho}{\rho}\right)=1.9\%$  found in [13].

As shown in Fig. 4.6, the amplitude of the AMR-effect increases approximately linearly with the layer thickness, before saturating at  $d=45 \text{ nm}$  where it remains constant apart from slight fluctuations due to uncertainties in the sample fabrication steps.<sup>1</sup> By averaging the AMR-amplitude-values of the saturation range mean values of  $\left(\frac{\Delta\rho}{\rho}\right)_{\text{long}}=(1.88 \pm 0.08)\%$  and  $\left(\frac{\Delta\rho}{\rho}\right)_{\text{trans}}=(1.92 \pm 0.11)\%$  are found which correspond quite nicely to the literature value of  $\left(\frac{\Delta\rho}{\rho}\right)=1.9\%$  given in [13].

<sup>1</sup> In the case of the 72 nm thick sample, for example, an imperfect lift-off process led to a partly damaged Hall-bar geometry, and thus a higher value of  $\rho_0$  which results in a lower AMR-amplitude in this case. However  $\rho_1$  remained unchanged.

Surprisingly, in Fig. 4.6, for almost all of the samples it is the case that the transverse data points lie slightly above the longitudinal ones. Since "pinning" effects that lead to a dependence of the AMR-amplitude on the applied external field  $H$  can be seen in the longitudinal in-plane measurements, but not in the transverse ones, it is tempting to assume that they are responsible for the difference in longitudinal and transverse AMR-amplitude. In order to test this hypothesis, this difference in amplitudes  $\Delta A_{\text{AMR}} = \left(\frac{\Delta\rho}{\rho}\right)_{\text{trans}} - \left(\frac{\Delta\rho}{\rho}\right)_{\text{long}}$  is calculated for two samples with thickness levels in the "saturation" range and one with a value of  $d$  within the "linear-increase" range for comparison for all of the applied magnitudes of  $H$ . The results of this procedure are plotted as a function of the applied external field in Fig. 4.7.



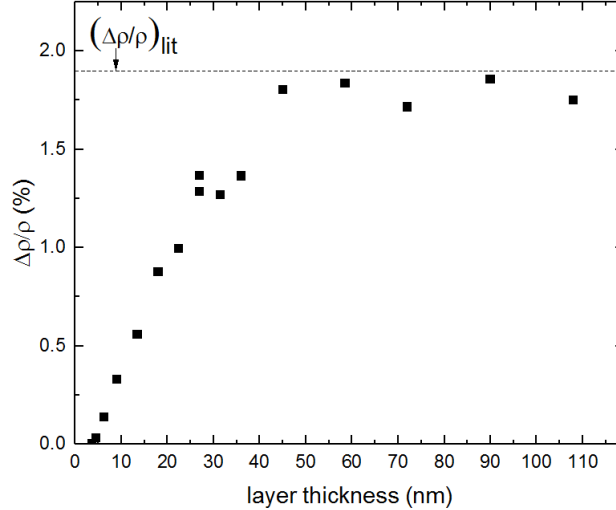
**Figure 4.7:** Difference of the longitudinal and transverse in-plane AMR-amplitudes  $A_{\text{AMR}}$  as a function of the external field for three samples of different thickness. Both the 90-nm and the 45-nm samples have AMR-amplitudes in the "saturation" range while the one with a layer thickness of 18 nm is in the "linear-increase"-range.

Figure 4.7 proves that this hypothesis is wrong. Only a very small decrease in  $\Delta A_{\text{AMR}}$  with increasing field strength can be seen due to decreasing "pinning" effects in all of the samples. However, its contribution is negligible. Hence, the difference in longitudinal and transverse amplitude of the AMR can be seen as independent of the magnetic field strength. As the difference between longitudinal and transverse amplitudes are much larger in the "saturation" range than in the "linear increase" range it is to some extent dependent on the layer thickness  $d$ . However, as one can see in Fig. 4.6, its value changes from sample to sample.

The origin of this phenomenon presumably lies within the structures of the domains that are forming within the ferromagnetic layer. Their size, alignment and behaviour at the domain walls might give rise to additional resistivity effects. In order to prove this hypothesis a Hall-bar with a different geometry must be fabricated in the future to determine the size of said domains as they would play a smaller role in larger Hall-bar structures and vice versa.

#### 4.1.4 Oopt-results

As previously explained in section 3.2.2, in out-of-plane measurements the Hall-bar orientated horizontally provides the oopt-geometry. Its longitudinal AMR-behaviour is depicted in Fig. 4.8 as a function of the sample thickness.



**Figure 4.8:** Behaviour of the longitudinal changes of resistivity amplitude due to the AMR-effect in oopt-geometry at 7 T as a function of the layer thickness of the samples together with its literature value.

Similarly to the in-plane case, the AMR-amplitudes in Fig. 4.8 show a linear increase up until  $d=45$  nm and no further change for thicker films. Generally, apart from both of the 27-nm-samples being situated at a slightly too high value, the data points of the samples also behave analogously. However, in this case the saturation value lies at  $(\frac{\Delta\rho}{\rho})_{\text{long}} = (1.80 \pm 0.06)$  % which is approximately 5% lower than both of its ip-values. As  $\rho_0$  remains nearly unchanged, its origin lies within a decrease in  $\rho_1$ -magnitude. This difference in amplitude can not be explained by the predictions of the first order model of the AMR, as according to Fig. 4.1,  $\rho_1$  should be equal in both of the geometries. However, higher order contributions of the AMR in single-crystalline ferromagnets might lead to a difference in ip and oopt amplitude.

Another possible explanation of this effect is the influence of the AHE. As discussed in section 2.3.2, different orientations of  $\mathbf{M}$  lead to the formation of spin accumulations on opposing sides of the Hall-bar which themselves can induce additional charge currents in parallel to the initial one, and therefore reduce the resistivity of the ferromagnetic layer dependent on the distance between them. In ip-geometry no spin-currents  $\mathbf{J}_s$  occur when  $\mathbf{H} \parallel \mathbf{j}$  as they scale with  $\mathbf{M} \times \mathbf{J}_q$ . However, when  $\mathbf{H} \parallel \mathbf{t}$  spin accumulations should occur on the top and bottom of the ferromagnet, and according to Eq. (2.15) due to its low thickness  $d$  cause the most dominant change in resistivity. For this reason, the angle-dependent-effects of the AHE enlarge the amplitude of the AMR the most in ip-geometry, whereas in the oopt for  $\mathbf{H} \parallel \mathbf{n}$  spin accumulations occur on both sides of the Hall-bar that are further apart by the width  $w$  than in the previous case, and for this reason cause a lower contribution to the amplitude.



### 4.1.5 Oopj-results

In (4.1.1) the assumption has been made that the angle-dependent change of longitudinal resistivity in the oopj-geometry occurs due to spin-accumulations on opposite sides of the sample caused by the AHE. This claim is supported by the position of the minimum values of the resistivity appearing at  $\mathbf{H} \parallel \mathbf{t}$  where the contribution of the AHE should be the most present. According to the theoretical equation (2.15) given in section 2.3.2, the measured amplitudes  $\left(\frac{\Delta\rho}{\rho}\right)$  should decrease with increasing layer thickness  $d$ . However, one has to consider some bulk effect as an ordered lattice of a ferromagnetic conductor requires a minimal thickness to develop. For this reason, it is assumed that for low values of layer thickness,  $\left(\frac{\Delta\rho}{\rho}\right)$  increases with  $d$  while behaving according to theory and hence decreases with increasing layer thickness. This theoretical prediction can now be compared to the experimentally determined dependence of  $\left(\frac{\Delta\rho}{\rho}\right)$  on  $d$  depicted in Fig. 4.9.

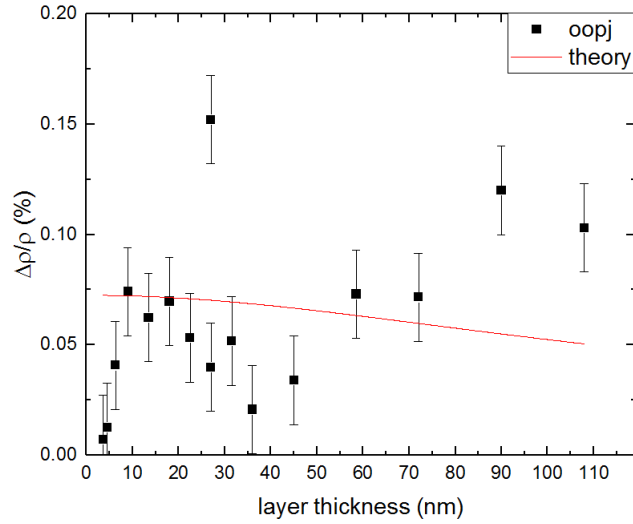


**Figure 4.9:** Behaviour of the longitudinal changes of resistivity amplitude in oopj-geometry at 7 T as a function of the layer thickness of the samples together with the theoretical contribution of the AHE for values of  $|m_t| = 1.0$ ,  $\beta = 0.8$ ,  $\zeta = 2.3$  which were chosen to receive a sufficient amplitude. For the other constants,  $\frac{\sigma_{\text{AHE}}}{\sigma}$  and  $\lambda_{\text{sf}}$ , the same values as in Fig. 2.12 were applied. The error bars of  $\left|\frac{\Delta\rho_1}{\rho_0}\right| = 2 \cdot 10^{-4}$  are selected according to the theoretical influence of a possible tilt on the amplitude  $\rho_1$  that can be found in the appendix B.

As it is shown in Fig. 4.9, the behaviour of the angle-dependent changes in longitudinal resistivity in the oopj-geometry greatly differs from both the ip- and oopt-cases. For one thing, its amplitude is one magnitude smaller. Additionally as expected, some sort of bulk effect can be seen for low values of  $d$  with  $\left(\frac{\Delta\rho}{\rho}\right)$  increasing with rising values of  $d$ . At  $d > 18$  nm, a decrease in amplitude is visible, however it is much steeper than predicted by the theory curve. Hence it becomes visible, that the assumptions of a constant spin diffusion length  $\lambda_{\text{sf}}$  and anomalous Hall angle  $\alpha_{\text{AHE}}$  are not valid in this experiment. This is confirmed in section 4.2, where it is found, that  $\alpha_{\text{AHE}}$  displays a rich dependence on  $d$  for low layer thicknesses. For values of  $d > 36$  nm, the subsequent increase of  $\left(\frac{\Delta\rho}{\rho}\right)$  does not agree with the theory curve with its data points fluctuating from sample to sample and rather showing an increase with rising layer thickness. For this reason, an additional effect of a higher magnitude than the contribution of the AHE must be present in the thicker samples.

Generally, most of the data points of the very thick samples lie above those of the thinner ones, apart from the first 27-nm-sample which has a rather unusually high magnitude of  $(\frac{\Delta\rho}{\rho})=0.15\%$ . In this case another measurement was conducted with the sample rotated by  $90^\circ$  to get the oopj-behaviour of the other Hall-bar, however its amplitude remained unchanged. This strange anomaly was the reason for the fabrication of a second sample of the same thickness to find out whether it is reproducible. As one can see in Fig. 4.9 this is not the case with its change in amplitude being situated at a much lower level. Apart from its unusually high longitudinal resistivity, no reason for this high value of  $(\frac{\Delta\rho}{\rho})$  could be found when looking for anomalies of the first 27-nm-sample, as its ip- and oopj-behaviour correspond to that of the second sample. One possible source of these strong fluctuations of the data-points might lie within a tilt when glueing the samples on the chip carrier or placing them on a dipstick, that can give rise to an additional misalignment-angle-dependent AMR contribution to  $\rho_{long}$  in oopj-geometry which might overshadow the AHE-contribution.

To test this hypothesis, the theoretical influence of a slightly rotated sample is investigated in the appendix B. Here only the results of this thought experiment are given. Assuming maximum misalignments of  $\alpha = 4^\circ$  in the  $\mathbf{j}$ - $\mathbf{t}$ -plane and  $\gamma = 4^\circ$  in the  $\mathbf{j}$ - $\mathbf{n}$ -plane and applying a maximum AMR-amplitude of cobalt of  $|\frac{\rho_1}{\rho_0}|=2.0\%$ , a maximal change of resistivity amplitude of  $|\frac{\Delta\rho_1}{\rho_0}|=0.02\%$  is found. Therefore error bars of this magnitude are also given in Fig. 4.9. However, it becomes clear that these tilt-effects do not have a sufficient amplitude to explain the found oopj-behaviour. Another potential explanation is the existence of crystalline ordered layers in the thicker samples which might have given rise to higher order AMR-contributions, which potentially led to the visible increase in oopj-amplitude for  $d>36$  nm.

For some samples two out-of-plane measurements were conducted to receive oopj-data for both of the Hall-bars. It was found that the values of  $(\frac{\Delta\rho}{\rho})$  also vary greatly from Hall-bar to Hall-bar within the same sample.<sup>2</sup> Hence it is assumed that due to these large fluctuations several measurements are necessary to deliver reliable data of the ADMR-effects in oopj-geometry in a ferromagnetic conductor. A reason for this might be fluctuations of layer thickness within a sample, the local formation of an ordered crystalline layer, non-linear temperature changes taking place during the measurement as well as so far unknown additional effects.

#### 4.1.6 Investigation of the possible contribution of higher order AMR-contributions

In this section, the previously mentioned possible influence of higher order AMR-contributions that need to be considered in crystalline ferromagnetic layers is investigated. Assuming a charge current along the  $[1\ 0\ 0]$ -crystal-direction of a cubic or tetragonal crystal lattice and taking the first order correction term into account, the change in resistivity due to the AMR can be written as [47]:

$$\rho_{long} = \rho_0 + \rho_1 \cdot m_j^2 + \rho_3 \cdot m_n^2 \quad (4.8)$$

This additional  $m_n^2$ -contribution to the AMR offers some explanation on the difference in ip and oopt-amplitude, as it would give rise to an additional  $\rho_3 \cos^2 \gamma$ -behaviour

<sup>2</sup>The sample with a thickness of 21.5 nm, for example, had oopj-amplitudes of  $(\frac{\Delta\rho}{\rho})=9.4 \cdot 10^{-4}$  for the upper Hall-bar and  $(\frac{\Delta\rho}{\rho})=1.5 \cdot 10^{-4}$  for the lower one. In Fig. 4.9 their mean value is depicted.

in oopt geometry, that counteracts the  $\rho_1 \sin^2 \gamma$ -dependence of  $m_j^2$  and lead to a decreased effective amplitude of  $(\rho_1 - \rho_3)$ , while the ip-amplitude remains unchanged. Furthermore it also causes a  $\rho_3 \cos^2 \beta$ -function in oopj-geometry and thus leads an AMR-contribution that would explain the sudden increase in  $(\frac{\Delta\rho}{\rho})$  seen in Fig. 4.9 in the oopj-data for the thicker samples  $d > 36$  nm.

In order to detect if and for what layer thicknesses  $d$  a crystalline order might have formed within the ferromagnetic layer, the measured ip, oopj and oopt-data are compared. Fig. 4.10(a) depicts both the relative AMR-amplitudes in ip and oopt-geometry, which should be equal on an amorphous ferromagnet. In Fig. 4.10(b), the sum of oopj- and oopt- $(\frac{\Delta\rho}{\rho})$  are depicted together with its in-plane value. According to Eq. (4.8) their combined change in resistivity is equal to the one in ip-geometry in a crystalline layer.

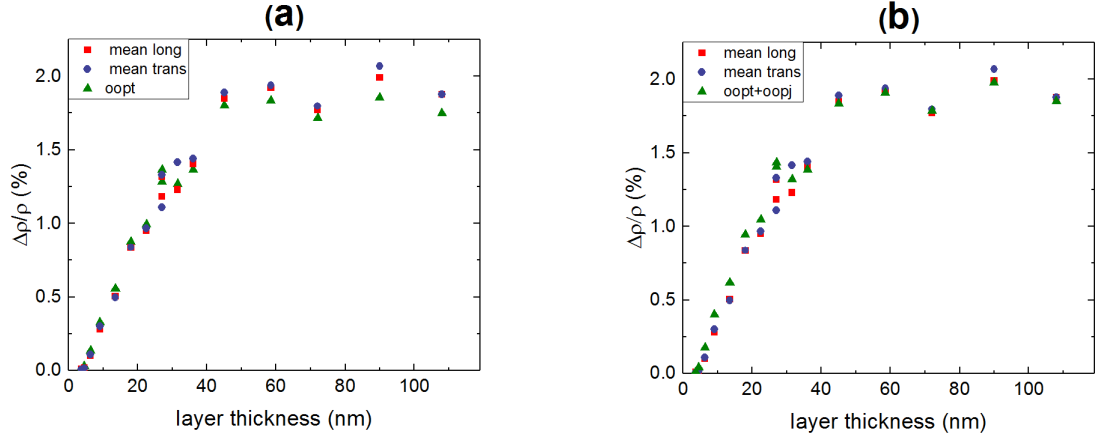


**Figure 4.10:** Comparison of the longitudinal relative changes of resistivity amplitude in ip- and oopt-geometry at 7 T as a function of the layer thickness of the samples. In (a) the case of an amorphous ferromagnet is investigated, by comparing oopt and ip, whereas in (b) it is tested to what extent the experimental data are in agreement with the theoretical predictions of a crystalline ferromagnetic layer.

As one can see in Fig. 4.10, the amorphous model corresponds to the experimental data up to approximately 36 nm with the oopt-data point being situated between the longitudinal and transverse ip-values. For higher values of  $d$ , however, rather the sum of oopj- and oopt-data is equal to the ip-amplitude, indicating the presence of an ordered, crystalline layer. This suggests that a crystalline order has formed in the thicker samples with  $d > 36$  nm.

To further confirm this assumption, the crystal-structure of the 72 nm-sample was investigated via XRD-scans, however, no reflections indicating an ordered crystalline lattice of the Co-layer were found. Nonetheless it may be possible that small crystalline areas have formed within the thicker samples, which could not be resolved in XRD scans. This is supported by the fact that on the one hand we find good experimental agreement of Fig. 4.10 to the theoretical predictions of the higher order AMR-contributions and on the other hand we observe a finite amplitude in the oopj-rotation plane for larger values of  $d$  that could neither be explained with misalignment-dependent AMR-contributions nor measurement errors. In addition, for lower values of  $d$ , the oopj-data in Fig. 4.15 behaves according to the enhanced theoretical AHE contribution.

## 4.2 Scaling behaviour of the anomalous Hall effect

As shown in the previous section, the theoretical predictions of the angle-dependent contribution of the AHE to the longitudinal resistivities do not correspond to the measurement results in oopj-geometry. This might originate from the scaling behaviour of the AHE as well as the dependence on its conductivity contribution  $\sigma_{\text{AHE}}$  on  $\sigma_{\text{long}}$  and hence the anomalous Hall angle  $\alpha_{\text{AHE}}$ , which is analyzed in this section.

### 4.2.1 Experimental determination of the transverse resistivity contribution of the AHE

The first step to determine the scaling behaviour of the AHE is to determine its transverse resistivity amplitude  $\rho_{\text{AHE}}$  in oopj and oopt-orientation. As explained in section 2.2.5.2 the total transverse resistivity in Hall experiments of ferromagnetic conductors can be written as the sum of the OHE- and AHE-resistivity contributions as given in Eq. (2.10).  $\rho_{\text{OHE}}$  varies linearly with the applied magnetic field strength  $H$ , while  $\rho_{\text{AHE}}$  changes much more steeply for low values of  $H$  and then saturates at a constant value for  $H > H_s$ . Upon plotting the amplitudes of the transverse changes in resistivity in oopj- and oopt-orientation for the five different applied magnetic field strengths applied in the measurements in Fig. 4.11, this behaviour can also be found within the thin film ferromagnetic cobalt samples fabricated in this thesis.

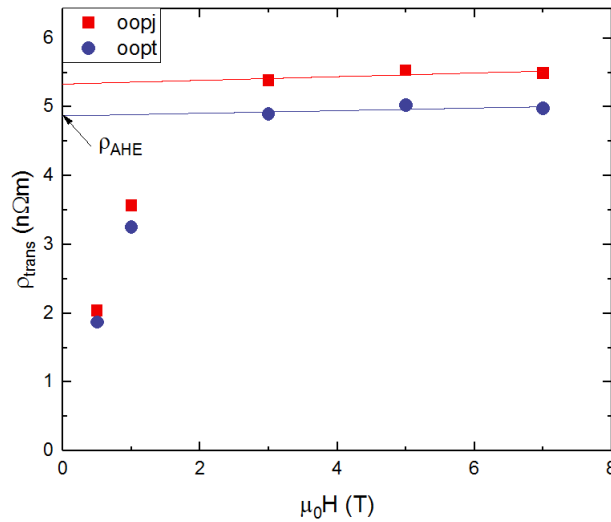


**Figure 4.11:** Anomalous Hall effect in a 6.3 nm-thick cobalt layer for both oopj and oopt-geometry. For high values of the magnetic field a small rise of  $\rho_{\text{trans}}$  can be seen due to the OHE. For  $H < 3$  T the steep change of the transverse resistivity of the AHE is visible in the data points at  $H=1$  T and  $H=0.5$  T. In order to determine  $\rho_{\text{AHE}}$ , a linear fit is applied through the three data-points at 3 T, 5 T and 7 T of the OHE-range.

As one can see in Fig. 4.11, the anomalous Hall results of the samples correspond quite nicely to the theoretical one depicted in Fig. 2.8 displaying both the steep increase of the AHE-range between the two data points of  $H=0.5$  T and  $H=1$  T as well as the OHE-range for larger values of  $H$ . The total contribution of the anomalous Hall effect can now be determined using a linear fit through the OHE-field-range of  $\rho_{\text{trans}}$  where its remaining change in resistivity occurs due to the ordinary Hall effect. By extrapolating this fit to  $H = 0$  T, the contribution of the OHE on  $\rho_{\text{trans}}$  is eliminated and  $\rho_{\text{AHE}}$  is equal to its intercept with the y-axis [19].

### 4.2.2 Thickness-dependent behaviour

By applying this method the amplitudes of the transverse resistivity due to the anomalous Hall effect were determined in oopj and oopt geometry for all of the fabricated samples and plotted against their layer thickness  $d$ . The result can be seen in Fig. 4.12.

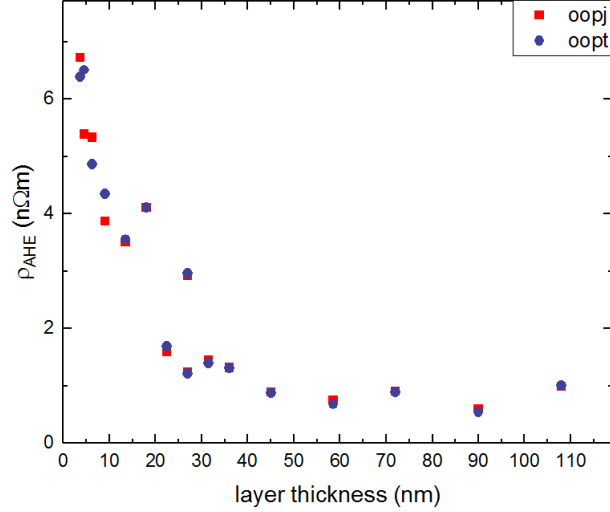


**Figure 4.12:** Experimental behaviour of the resistivity contribution of the AHE  $\rho_{\text{AHE}}$  as a function of the layer thickness  $d$  of the samples in both oopj and oopt geometry.

In Fig. 4.12 it becomes apparent that  $\rho_{\text{AHE}}$  decrease with increasing layer thickness for both oopj- and oopt-geometry. Fluctuations between their amplitudes only occur at low thickness values, however the average relative errors of the fits are of the magnitude  $\Delta\rho_{\text{AHE}} \approx (1-2)\%$  and are hence not large enough to explain them. Both the data-points of the 27 nm-(1) sample and the 18 nm one are situated at a value that is too high. While the former has already previously showcased strange behaviour, the results of the latter have been normal so far. The 27 nm-(2) sample has a much lower value of  $\rho_{\text{AHE}}$ , which indicates that some unknown error might have occurred in the fabrication of the first sample. However, errors in the extraction of  $\rho_{\text{AHE}}$  are much more likely than in the previous results due to its determination method by fitting a line through three data points.

Generally,  $\rho_{\text{AHE}}$  shows a thickness-dependent behaviour that is very similar to that of  $\rho_{\text{long}}$  depicted in Fig. 4.7 which indicates that there is a correlation between these two values.

### 4.2.3 Experimental scaling behaviour

In order to quantify this correlation and compare it to the results of previous experiments depicted in Fig. 2.9, the conductivity is calculated from the resistivity for both  $\rho_{\text{AHE}}$  and  $\rho_{\text{long}}$ . Assuming  $\rho_{\text{long}} \gg \rho_{\text{trans}}$ , their conductivities can be determined by the following equations.

$$\sigma_{\text{long}} = \frac{1}{\rho_{\text{long}}} \quad (4.9)$$

$$\sigma_{\text{AHE}} = \left| \frac{-\rho_{\text{AHE}}}{\rho_{\text{long}}^2} \right| \quad (4.10)$$

The scaling behaviour of the AHE can now be determined by plotting  $\sigma_{\text{AHE}}$  as a function of  $\sigma_{\text{long}}$ . As confirmed by previous experimental publications [31] it is expected that according to the bad-metal-hopping regime, a rise of  $\sigma_{\text{AHE}}$  with  $\sigma_{\text{long}}$  of the amplitude  $\sigma_{\text{AHE}} \sim \sigma_{\text{long}}^{1.6-1.8}$  will occur in the range  $\sigma_{\text{long}} < 10^4(\Omega\text{cm})^{-1}$ . For higher values of  $\sigma_{\text{long}}$ ,  $\sigma_{\text{AHE}}$  should remain constant in the good-metal regime in  $10^4(\Omega\text{cm})^{-1} \leq \sigma_{\text{long}} \leq 10^6(\Omega\text{cm})^{-1}$ . It is expected that none of the samples fabricated in this thesis are situated within the high conductivity regime  $\sigma_{\text{long}} > 1 \cdot 10^6(\Omega\text{cm})^{-1}$  [31].

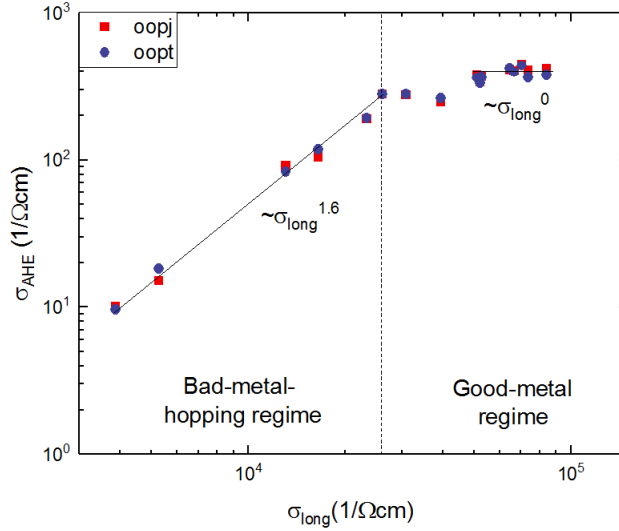


**Figure 4.13:** Experimental behaviour of the transverse conductivity due to the anomalous Hall effect  $\sigma_{\text{AHE}}$  as a function of  $\sigma_{\text{long}}$  in oopj and oopt geometry. Both the characteristic behaviour of the bad-metal-hopping regime and the good-metal-regime can be seen.

As shown in Fig. 4.13,  $\sigma_{\text{AHE}}$  rises with  $\sigma_{\text{long}}$  up until approximately  $\sigma_{\text{long}} < 3 \cdot 10^4(\Omega\text{cm})^{-1}$ , which corresponds well to its expected behaviour in the bad-metal-hopping-regime and shows no change for increasing values of  $\sigma_{\text{long}}$  as expected in the good-metal-regime. The samples with  $d \leq 21.5$  nm are situated in the bad-metal-hopping regime, while those with  $d > 21.5$  nm are all in the range of the good-metal regime. None of the samples has a conductivity  $\sigma_{\text{long}} > 1 \cdot 10^6(\Omega\text{cm})^{-1}$  so the high-conductivity regime cannot be seen in Fig. 4.13.

By conducting a fit of the form

$$\sigma_{\text{AHE}} = C \cdot \sigma_{\text{long}}^{\alpha} + D \quad (4.11)$$

through the data points of the bad-metal-hopping regime, its scaling behaviour  $\alpha$  can be determined.

The conducted fit yields  $\alpha = 1.6 \pm 0.3$  for both oopj- and oopt-geometry which is in good agreement with its literature value of  $\alpha = 1.6-1.8$  found in [31]. In order to further investigate the angle-dependent contribution of the AHE, the anomalous Hall angle  $\alpha_{\text{AHE}} = \frac{\sigma_{\text{AHE}}}{\sigma_{\text{long}}}$  is plotted as a function of the layer thickness of the samples in Fig. 4.14.

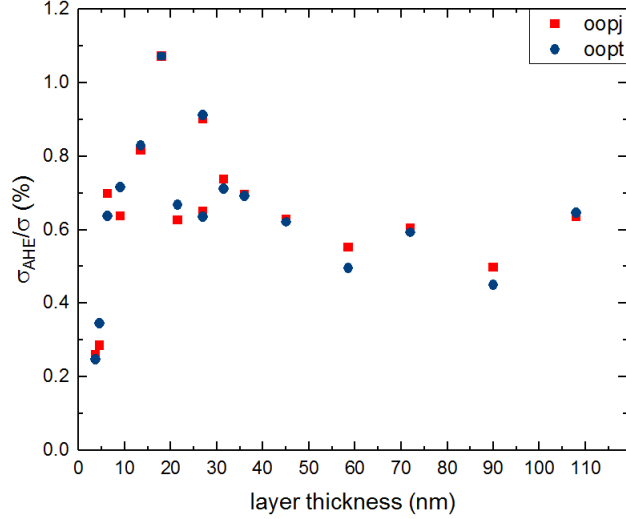


**Figure 4.14:** Experimental behaviour of the anomalous Hall angle  $\frac{\sigma_{\text{AHE}}}{\sigma_{\text{long}}}$  as a function of the layer thickness  $d$ .

As shown in Eq. (2.15), the change in longitudinal resistivity due to the AHE scales with  $\alpha_{\text{AHE}}^2$ . Therefore higher values of the anomalous Hall angle should lead to bigger values of  $\left(\frac{\Delta\rho}{\rho}\right)$  in the oopj-geometry, assuming the AHE is the dominant effect in this geometry. In Fig. 4.14,  $\alpha_{\text{AHE}}$  first rises with increasing layer thickness for low magnitudes of  $d$  up to a maximum value at  $d=18$  nm is reached and then drops to a value of  $\alpha_{\text{AHE}} \approx 0.6\%$  that is nearly constant, apart from slight fluctuations at  $d=72$  nm and  $d=58.5$  nm.

According to this experimental result, the ADMR-contribution of the AHE first increases with growing layer thickness due to the thickness-dependence of  $\alpha_{\text{AHE}}$  and the geometric thickness scaling, as it has been assumed in section 4.1.5 and after reaching a maximum at  $d=18$  nm decreases with rising values of  $d$  as depicted in Fig. 4.15 due to an almost constant  $\alpha_{\text{AHE}}$ . Taking into account the experimental layer-thickness-dependent values of  $\alpha_{\text{AHE}}$ , another theory-curve of the contribution of the AHE is plotted together with the measured oopj- $\left(\frac{\Delta\rho}{\rho}\right)$  in Fig. 4.15. For the theory curve, the same values of  $|m_t| = 1.0$ ,  $\beta = 0.8$ ,  $\zeta = 2.3$  and  $\lambda_{\text{sf}} = 40$  nm as in Fig. 4.9 were chosen.

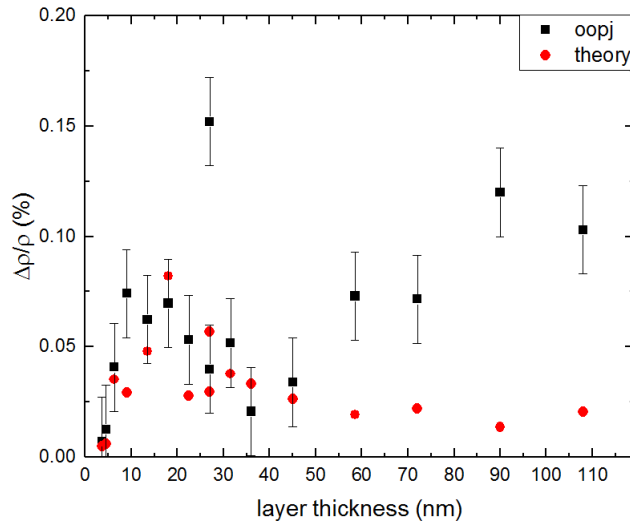


**Figure 4.15:** Behaviour of the longitudinal changes of the resistivity amplitude in oopj-geometry at 7T as a function of the layer thickness of the samples together with an adapted theory curve calculated with the measured  $\alpha_{\text{AHE}}$ -values.

With the improved theory curve in Fig. 4.15, the expected increase for low values of  $d$  becomes visible. Its general behaviour is now in satisfactory agreement to the experimental results up until  $d=45$  nm, displaying both an increase with  $d$  for  $d \leq 18$  nm and a steeper decrease for  $d > 18$  nm that corresponds to the experimental results. For larger values of the layer thickness however, it still does not offer any explanation for the visible increase in oopj-amplitude. This supports the assumption that the oopj-behaviour for  $d > 36$  nm can not be explained with the angle-dependent contribution of the AHE but rather has a different origin like for example the potential formation of a crystalline-oriented layer in the thicker samples.

### 4.3 Unidirectional spin Hall magnetoresistance

So far, only the ADMR-effect of ferromagnetic conductors have been explored. To conclude the results of this thesis, we will now expand our research to the effects taking place at the interface of a FM|NM-sample. Besides examining the contributions of the well known SMR effect, it will be investigated, whether the newly discovered unidirectional Spin Hall magnetoresistance (USMR) can be detected in a cobalt|platinum bilayer with the normal Hall-bar geometry.

#### 4.3.1 Theoretical background

As previously stated in section 2.3.1, in NM-FMI-interfaces an angle-dependent contribution to the resistivity appears due to spin currents being able to partly enter the ferromagnet dependent on the angle between their spin alignment and the magnetization of the FM. Recently it has been discovered, that in heavy NM/Co-bilayers (e.g. NM=Pt, Ta and W) an additional change of the longitudinal resistance is found upon reversing the polarity of the current or the sign of the magnetization [48]. This so-called unidirectional spin Hall magnetoresistance effect is linearly dependent on the applied current density and has opposite signs in Ta and Pt [49]. The detected amplitude of this change has been estimated at  $(0.002-0.003)\%$  of the total resistance for an applied current density of  $j = 10^7$  A/cm<sup>2</sup>. Due to its symmetry as well as material dependent sign



it is assumed that the scalar product of the magnetization  $\mathbf{M}$  with the SHE-induced spin accumulations at the FM/NM-interface ( $\mathbf{J}_q \times \mathbf{z}$ ), create a magnetoresistance contribution of the form  $\mathbf{J}_q \times \mathbf{M}$ , which gives rise to the USMR as illustrated in Fig. 4.16.

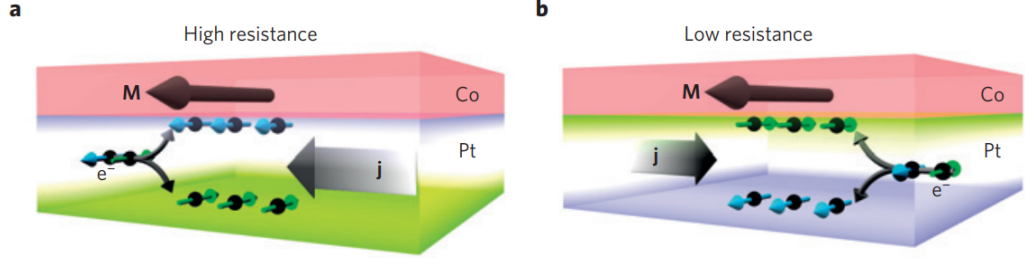


**Figure 4.16:** Illustration of the USMR in a Pt|CO-interface layer. In (a) the parallel alignment of the spin induced spin accumulations ( $\mathbf{J}_q \times \mathbf{z}$ ) and  $\mathbf{M}$  lead to an increase in resistance  $R$ , whereas in (b) an antiparallel alignment leads to a drop of  $R$ . Taken from [49].

### 4.3.2 Additional ADMR-measurements

In order to investigate this effect a sample containing a layer of platinum with a thickness of 4.5 nm deposited on top of a 9 nm thick cobalt layer is fabricated via electron-beam evaporation (EVAP). Subsequently an ADMR-measurement at room temperature using the same angular step-width is conducted in each of the three different measurement geometries. In this case both SMR and AMR effects need to be considered. By applying the relation  $m_j^2 + m_t^2 + m_n^2 = 1$ , their combined influence on the resistivity behaviour can be written as:

$$\rho_{\text{long}} = \rho_0 + (\rho_1^{\text{AMR}} + \rho_1^{\text{SMR}})m_j^2 + \rho_1^{\text{SMR}}m_n^2 \quad (4.12)$$

$$\rho_{\text{trans}} = (\rho_1^{\text{AMR}} + \rho_1^{\text{SMR}})m_j m_t + (\rho_2^{\text{AMR}} + \rho_2^{\text{SMR}})m_n \quad (4.13)$$

In Table 4.2 these changes in resistivity induced by the AMR and SMR are listed in each of the three different measurement geometries.

	ip	oopj	oopt
$\rho_{\text{long}}$	$\rho_0 + (\rho_1^{\text{AMR}} + \rho_1^{\text{SMR}}) \cos^2 \alpha$	$\rho_0 + \rho_1^{\text{SMR}} \cos^2 \beta$	$\rho_0 + \rho_1^{\text{SMR}} + \rho_1^{\text{AMR}} \sin^2 \gamma$
$\rho_{\text{trans}}$	$(\rho_1^{\text{AMR}} + \rho_1^{\text{SMR}}) \cos \alpha \sin \alpha$	$(\rho_2^{\text{AMR}} + \rho_2^{\text{SMR}}) \cos \beta$	$(\rho_2^{\text{AMR}} + \rho_2^{\text{SMR}}) \cos \gamma$

**Table 4.2:** Theoretical ADMR-behaviour of  $\rho_{\text{long}}$  and  $\rho_{\text{trans}}$  in the three possible measurement geometries.

It becomes apparent, that the expected changes in resistivity in the presence of both AMR and SMR effects either lead to an increased longitudinal (transverse) ADMR amplitude if both  $\rho_{1,(2)}^{\text{AMR}}$  and  $\rho_{1,(2)}^{\text{SMR}}$  have the same sign and a decrease for opposite signs. The main difference to previous measurements is the presence of a  $\cos^2 \beta$ -function in oopj-geometry. However, apart from this, the experimental results look just like those of the Co-samples depicted in Fig. 4.3 and 4.4 and for this reason they have been placed in the appendix C. Generally the results correspond to the theoretical predictions of Tab. 4.2. By fitting Eq. (4.3) to the longitudinal data, the value of  $(\frac{\Delta \rho}{\rho})$  can be determined and compared to previous results.

As shown in Tab. 4.2, in oopt-geometry the change in  $\rho_{\text{long}}$  is only dependent on the AMR-effect. Upon adding the data point of the Co|Pt-sample to the existing plot of the oopt-amplitudes as a function of  $d$  in Fig. 4.17, this is confirmed, as the new data point is situated at a similar value to the one of the 9-nm-sample containing the same layer thickness of cobalt. The value of the AMR-contribution in this sample is  $\left|\frac{\rho_1}{\rho_0}\right|^{\text{AMR}} \approx 0.306\%$ .

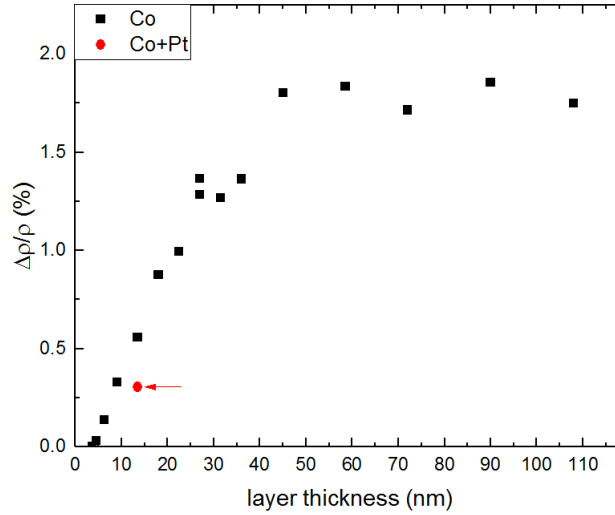


**Figure 4.17:** Behaviour of the longitudinal changes of resistivity amplitude due to the AMR-effect in oopt-geometry at 7 T as a function of the layer thickness of the co-samples as well as the Co|Pt-sample. For the latter  $d=13.5$  nm is chosen, which is the sum of the cobalt and platinum layer thickness.

In oopj-geometry however, the change in resistivity in the Co|Pt-sample should only be based on the SMR-effect, neglecting the influence of a possible tilt. By once again adding its change in amplitude in oopj-geometry as a function of  $d$  to the existing data in Fig. 4.18, a value of  $\left|\frac{\rho_1}{\rho_0}\right|^{\text{SMR}} \approx 0.174\%$  can be found. The angle-dependent contribution of the AHE is different in this case, as the spin accumulations of the FM can partly enter the NM layer. Hence they only form on the bottom side of the FM layer and its resistivity contribution can not be described with Eq. (2.15).

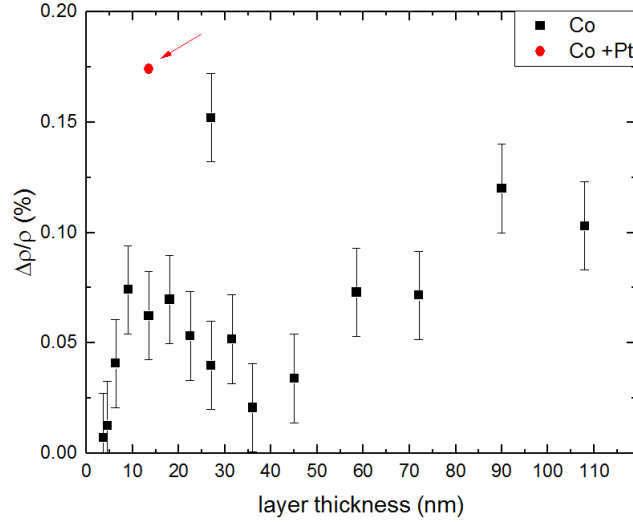


**Figure 4.18:** Behaviour of the longitudinal changes of resistivity amplitude in oopj-geometry at 7 T as a function of the layer thickness of the Co-samples as well as the Co|Pt-sample. The latter is plotted without error bars for greater clarity.

When adding the longitudinal and transverse in-plane data points to the given plot, it is found that they are both situated at approximately the same level as the 13.5-nm sample at a value of  $|\frac{\rho_1}{\rho_0}| \approx 0.460\%$ , being in good agreement with the assumption, that the contributions of the AMR and SMR add in this geometry. Furthermore it proves that the depicted oopj-contribution of the Co|Pt-sample in Fig. 4.18 is mostly caused by the SMR and a possible tilt only plays a minor role. Additionally, it leads to the conclusion, that the AHE-geometry in a FM-NM-bilayer is negligible as the spin accumulations can only form on one side of the FM layer. Corresponding to previous experimental results, the transverse results are approximately 5% larger than in the longitudinal case.

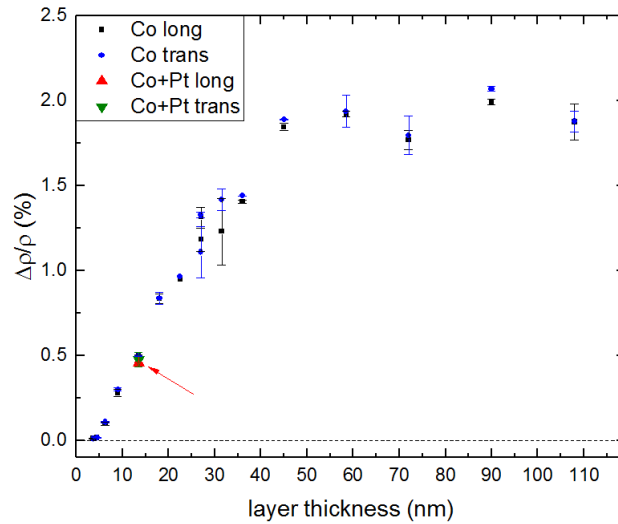


**Figure 4.19:** Depiction of the dependence of the longitudinal and transverse change in resistivity of the Co-samples of the layer thickness due to the AMR-effect in in-plane-geometry for a magnetic field of 7 T as well as due to the combined contribution of the AMR and SMR effect in the Co|Pt-sample.

### 4.3.3 Attempts to detect the USMR in the Co|Pt-boundary layer

In order to detect the USMR, in-plane ADMR measurements with a DC-current sweeping between positive and negative polarity, an increased digital filter count of 40 instead of 10 of the nanovoltmeters as well as a reduced step width of  $5^\circ$  were conducted. To measure both the differential resistance  $r$  as well as the curvature  $\kappa$  of the resistance, the current  $I_0$  was also modulated by  $\Delta I$  in the form  $\pm I_0 \pm \Delta I$ . There are two possible ways to evaluate the measurement data, one of which requiring the differential resistance. However, in this thesis an approach similar to the one applied by Olejník et. al. [50] has been chosen, while the method requiring the differential resistance is shortly illustrated in the Appendix D.

As previously stated, high current densities  $j$  are required to detect the USMR-effect. In the case of Avcı et al.  $j = 10^7$  A/cm<sup>2</sup> has been used [49]. In this thesis, ADMR-measurements were conducted with a maximum current of  $I_0=25.0$  mA ( $\Delta I = 2.5$  mA), which creates a current density of  $j \approx 2.3 \cdot 10^6$  A/cm<sup>2</sup> in the used Hall-bar geometry with a width of  $w=80$   $\mu$ m and a thickness  $d=13.5$  nm. Large values of  $j$  can lead to a change in the measured voltage due to an emerging vertical temperature gradient  $\nabla T$  within the Hall-bar structure because of the different conductivities in the FM and the NM layer, which needs to be considered. Conducting a Taylor series up to the second order, the measured voltage  $V$  can be written as:

$$V(I) = R(I)I + SI^2 \quad (4.14)$$

Here  $R(I)$  is the resistance of the conductor given as a function of  $I$  to emphasize its dependence on the polarity of the current. The term  $S$  describes an additional contribution to the voltage caused by the temperature gradient  $\nabla T||z$ , which gives rise to the spin Seebeck effect (SSE) [51, 52] in paramagnetic layers in contact with a FM and the anomalous Nernst effect (ANE) [53] in ferromagnetic layers. Both of said effects create an additional voltage  $j^2(\mathbf{M} \times \nabla T)$ , whose contribution scales with  $I_0^2$ , similar to the USMR. Dependent on the magnetization orientation, this additional voltage either enhances or lowers the measured voltage and thus effectively mimics the USMR-effect [49, 50].

In order to eliminate this contribution of the temperature gradient, the following formula is applied.

$$V_{\text{avg}} = \frac{V(I) - V(-I)}{2} = \frac{R(I) + R(-I)}{2} \cdot I \quad (4.15)$$

This equation should deliver the mean AMR-contribution of the sample and depict no signs of USMR nor the temperature dependent effects being a mean value of both polarities [50].

To detect the USMR and the polarity-dependent contributions of the SSE and ANE, the difference of voltage between both current signs  $\pm I_0$  is calculated.

$$V_{\text{diff}} = \frac{V(I) + V(-I)}{2} = SI^2 + \frac{R(I) - R(-I)}{2} \cdot I \quad (4.16)$$

Applying this formula on the experimental data, an oscillating behaviour of the USMR in  $V_{\text{diff}}$  should be visible. In order to detect the contribution of only the USMR, Olejník et al. plotted both the longitudinal and transverse changes in  $V_{\text{diff}}$ . In the transverse orientation, the angular dependence of the voltage is only caused by the thermal gradient

and therefore its amplitude can be quantified. By subtracting this value scaled by the geometric factor  $l/w$  from the longitudinal results, the amplitude of the USMR could be determined. For comparison, their results are depicted in Fig. 4.20.

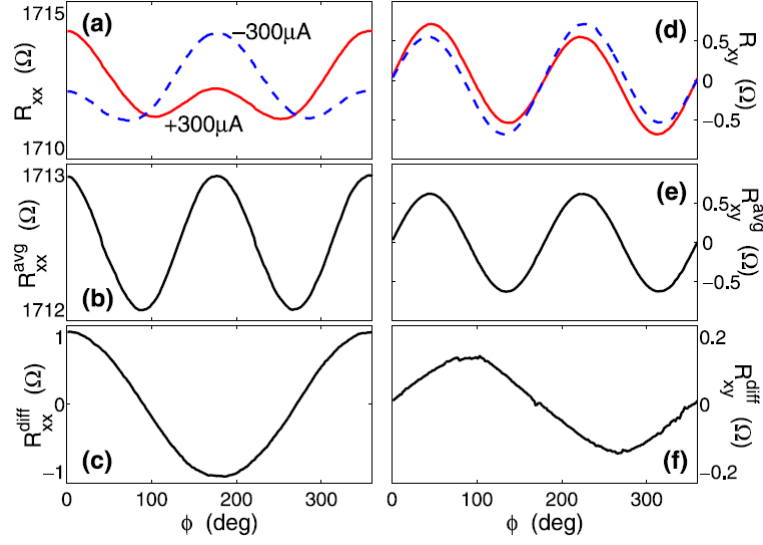


**Figure 4.20:** in-plane ADMR-measurement results of (Ga,Mn)As epilayers at an applied current of  $\pm 300 \mu A$ , 0.5 T and 130 K. In (a) and (d), the total change in longitudinal and transverse resistance due to AMR, SMR and USMR is illustrated for both polarities, whereas the depiction of  $R_{\text{avg}}$  in (b) and (e) singles out the contributions of the AMR and SMR in longitudinal and transverse direction. In (f) the transverse angle-dependent contributions of the thermal gradient  $\nabla T$  is given in. Its contribution has been removed from the longitudinal results in (c). Consequently, the remaining  $\cos \alpha$ -behaviour of  $R_{\text{diff}}$  in (c) is caused by the USMR. Taken from [50].

Due to the large USMR-amplitude of 0.2% in (Ga,Mn)As epilayers, its influence is already visible in the raw ADMR-data. When isolating its contribution, it is found that the USMR gives rise to a  $\cos \alpha$ -like behaviour.

In comparison, the angular dependence of  $V_{\text{avg}}$  measured in our experiment, is depicted in Fig. 4.21.

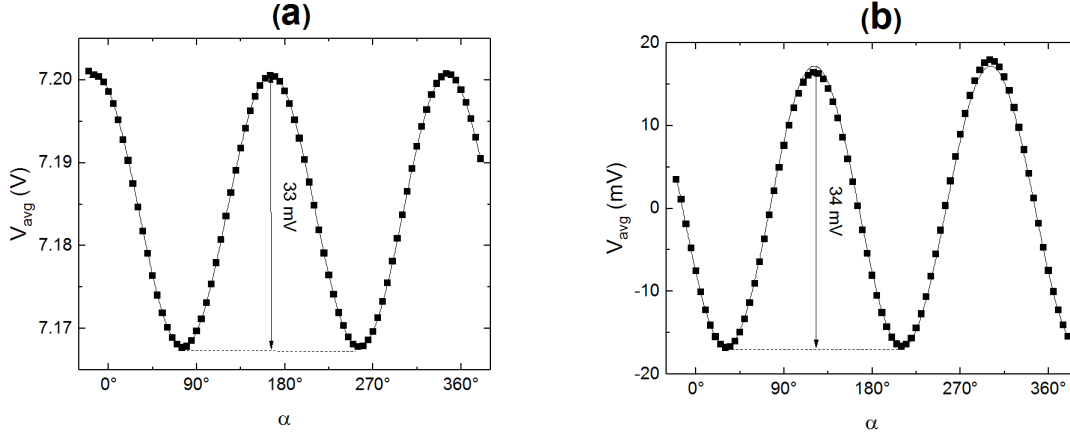


**Figure 4.21:**  $V_{\text{avg}}$  as a function of the angle  $\alpha$  in longitudinal (a) and transverse (b) direction. For comparison, the transverse voltage was scaled by the geometric factor  $l/w$  for better comparison. The visible  $\cos^2 \alpha$ -behaviour in (a) and  $\sin \alpha \cos \alpha$ -behaviour in (b) is caused by the AMR and SMR.

As seen in Fig. 4.21, the curvature of  $V_{\text{avg}}$  only consists of the even contributions of AMR and SMR to the voltage, also showing its previously determined amplitude.

In the applied in-plane geometry, the contributions of the USMR should be visible at  $90^\circ$ , with the spin accumulations ( $\mathbf{J}_q \times \mathbf{z}$ ) being antiparallel to  $\mathbf{M}$  (see Fig. 3.5), which leads to a decrease in voltage according to Fig. 4.16, whereas for  $270^\circ$  their parallel alignment increases  $V$ . Hence in this experiment, a  $\sin \alpha$ -behaviour of the USMR, as well as the thermal effects is expected to be visible in the longitudinal data. In order to better compare the longitudinal and transverse contributions of the USMR, ANE and SSE, the influence of the geometry is removed by calculating the electric field strength  $E_{\text{diff}}$  out of  $V_{\text{diff}}$  by the following formulae .

$$E_{\text{diff}}^{\text{long}} = \frac{V_{\text{diff}}^{\text{long}}}{l} \quad (4.17)$$

$$E_{\text{diff}}^{\text{trans}} = \frac{V_{\text{diff}}^{\text{trans}}}{w} \quad (4.18)$$

The longitudinal and transverse electric field strengths as a function of the angle  $\alpha$  are depicted in Fig. 4.22. Assuming a linear scaling behaviour of the USMR and a maximal change of 0.0015% based on the results in [49], its maximal amplitude  $A_{\text{USMR}} \approx 0.02 \text{ V/m}$  in this experiment<sup>3</sup> is also given in Fig. 4.22(a).

<sup>3</sup>The USMR scales linearly with  $j$ , thus the maximal change of 0.0015% given by Avci et. al has to be scaled by the factor  $j_{\text{exp}}/j_{\text{Avci}} \approx 0.23$  in this experiment. As given in Fig. 4.21, the average longitudinal voltage  $V_{\text{avg}} \approx 7.17 \text{ V}$  and hence the average longitudinal electric field  $E_{\text{avg}} \approx 12 \text{ kV/m}$ . Taking these parameters into account, the USMR should give rise to a  $\sin \beta$ -function of the amplitude:  $A_{\text{USMR}} = 0.0015\% \cdot 0.5 \cdot 0.23 \cdot 12 \text{ kV/m} \approx 0.02 \text{ V/m}$

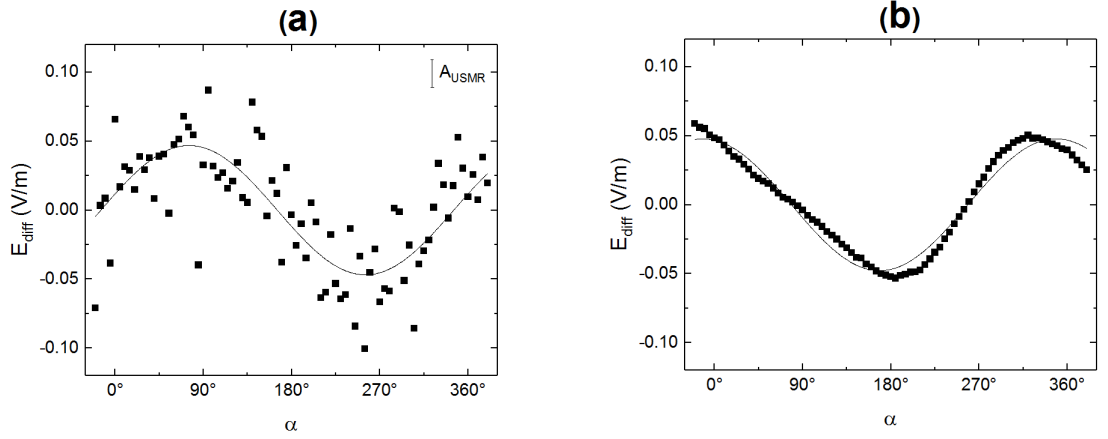


**Figure 4.22:**  $E_{\text{diff}}$  as a function of the angle  $\alpha$  in longitudinal (a) and transverse (b) direction. In (a), the USMR is expected to give rise to a cos-function of the amplitude  $A_{\text{USMR}}$ , while (b) enables the determination of the influence of the SSE and ANE effects. The offsets of both curves have been corrected for better comparison.

Upon comparing the amplitudes of Fig. 4.22(a) and (b) it becomes apparent that the contributions of the thermal gradient entirely overshadow any trace of a possible USMR-influence as both longitudinal and transverse results are identical. To prove this assumption, both curves are fitted with a sin-function in Origin. It is found that their amplitudes  $A_{\text{long}} = (0.047 \pm 0.005)$  V/m and  $A_{\text{trans}} = (0.048 \pm 0.001)$  V/m are equal within the given error range. Furthermore, the fluctuations of the longitudinal data points are of the same magnitude as the estimated amplitude of the USMR.

From these experiments, one can conclude that the geometry of the applied Hall-bar structure is too wide to detect the USMR. Therefore the necessary current of  $I_0 = 25$  mA to achieve the required current density  $j$  in this thesis is much larger than in the measurements of Olejník et. al. ( $300 \mu\text{A}$ ) [50] and Avci et. al. (8.5 mA) [49] and thus creates larger heating effects that are visible in the fluctuations of the data points. By using a geometry with a smaller width, proportionally lower currents are required and the distribution of the data points could be less altered by heating. Furthermore, the applied bilayer of Co|Pt differs from the trilayer used by Avci et. al., with Pt at the bottom, followed by layers of Co and  $\text{AlO}_x$ . This might have played a role, as Avci claims, that the temperature gradient in a NM|FM-bilayer is more pronounced when the conductivity of the top layer is larger than that of the bottom layer [48], which is the case in the sample prepared in this thesis and might have further enhanced the amplitudes of the temperature gradient driven effects SSE and ANE.





# Chapter 5

## Summary

Over the course of this chapter, the most important results of this thesis are firstly summarized and a quick outlook is given on further experiments in this field that need to be conducted to tie up some loose ends that could not be investigated in the framework of this thesis. Particularly the AHE and the recently discovered USMR [49] hold great promise for the future fabrication of spintronic devices, some of which will be described.

### 5.1 Conclusion and outlook

To put it in a nutshell, in the framework of this thesis the AMR-behaviour of metallic, ferromagnetic thin films in dependence of their thickness  $d$  was systematically studied. Thin films of cobalt with varying layer thickness were fabricated and ADMR-measurements were conducted in ip, oopj and oopt-geometry for different values of magnetic field strength. In order to determine their relative change in longitudinal resistivity due to the AMR-effect, the obtained data were fitted with  $\sin^2$ -functions and the extracted parameters were plotted as a function of the layer thickness for each of the three possible rotation geometries. As a first check, the role of interface scattering was analyzed by investigating the change in mean longitudinal resistivity as a function of  $d$  and fitting the data to a theoretical model. Indeed, interface scattering due to surface roughness plays an important role in our samples.

In in-plane-geometry both the changes in amplitude of the longitudinal and transverse resistivity show the same trend firstly increasing linearly with  $d$  and then saturating at mean values of  $\left(\frac{\Delta\rho}{\rho}\right)_{\text{long}} = (1.88 \pm 0.08)\%$  and  $\left(\frac{\Delta\rho}{\rho}\right)_{\text{trans}} = (1.92 \pm 0.11)\%$ . These saturation values are in good agreement with previous experimental results [13]. As a next step, it was investigated whether the slight difference in magnitude between the longitudinal and transverse  $\left(\frac{\Delta\rho}{\rho}\right)$  could be explained by magnetic domain pinning effects present in the longitudinal results, but absent in the transverse data. To this end, the difference in amplitude was plotted against the magnetic field strength applied in the ADMR-measurements. It was found that this difference did not scale with the magnetic field strength, but rather with the layer thickness with larger values of  $\Delta A_{\text{AMR}}$  occurring for larger values of  $d$ . However, its value also fluctuates from sample to sample. It is assumed that the difference between longitudinal and transverse amplitude appears due to the formation of magnetic domains within the ferromagnetic samples, whose size, walls and alignment might have had an effect on the resistivity. In the future the ADMR-effect of Hall-bar structures of different scales will have to be investigated in order to find out whether said difference in amplitude scales correspondingly.

The observed behaviour of the relative magnetoresistance in the oopt-rotation plane was very similar to the one found in ip-geometry increasing linearly with the layer thickness for low values of  $d$  and saturating at a constant value of  $\left(\frac{\Delta\rho}{\rho}\right)_{\text{long}} = (1.80 \pm 0.06)\%$

which is lower than in ip-geometry. One possible explanation for this difference is a lower amplitude of the additional angle-dependent contribution of the anomalous Hall effect in this geometry. Furthermore, higher order terms of the longitudinal resistivity might have contributed to this inequality. An investigation of another ferromagnetic material like, for example, nickel is necessary in order to find out whether this difference is material-dependent or an intrinsic property of the AMR.

The amplitudes extracted in the oopj-geometry exhibited a rich thickness dependence. While, corresponding to the angle dependent AHE-contribution for low layer thickness levels a decrease in  $\left(\frac{\Delta\rho}{\rho}\right)$  is visible, its magnitude is much larger than predicted by the theoretical model. Consequently, it was assumed, that the assumption of a constant spin diffusion length  $\lambda_{sf}$  and anomalous Hall angle  $\alpha_{AHE}$  is not valid in this experiment and a more elaborate theoretical model is required. The behaviour for large thicknesses is rather surprising. However, it can generally be stated that samples with larger values of  $d$  tend to have larger amplitudes which does not correspond to the predicted angle-dependent contribution of the AHE. Subsequently, the effect of a possible tilt in the rotation-plane on the oopj-amplitudes was investigated. Its maximal contribution was estimated to be  $\left|\frac{\rho_1}{\rho_0}\right|=0.02\%$  and is thus not large enough to explain the observed effect. As measurement results fluctuated from sample to sample and even from Hall-bar to Hall-bar within the sample, it is assumed, that the real oopj-behaviour for  $d>36$  nm is overshadowed by sample-dependent contributions like the randomized formation of crystalline layers in the thicker samples, which can cause higher order AMR-contributions. This claim needs to be investigated by future AMR-measurements of other ferromagnetic materials with a lower AMR-amplitude like iron (Fe) in order to reduce said higher-order AMR-contribution in this geometry as well as its potential tilt contributions.

Apart from the AMR, another effect that is present in ferromagnetic metals is the anomalous Hall effect. By plotting the out-of-plane amplitudes of the transverse resistivities of the samples as a function of the external magnetic field and fitting a straight line through the OHE-range, the contribution of the AHE  $\rho_{AHE}$  to  $\rho_{trans}$  was determined. The extracted AHE-amplitudes were then plotted against the layer thickness  $d$  and it was found that their their thickness dependence is very similar to that of the longitudinal resistivity. In order to investigate said correlation, the conductivity of the AHE was plotted as a function of the longitudinal conductivity. In the resulting Fig. 4.13,  $\sigma_{AHE}$  first rises with  $\sigma_{AHE} \propto \sigma_{long}^{1.6\pm 0.3}$  up until  $\sigma_{long} = 3 \cdot 10^4 (\Omega\text{cm})^{-1}$  and saturates for higher  $\sigma_{long}$ . This trend nicely agrees with previous experimental results of the scaling behaviour of the AHE in the bad-metal-hopping regime and in the good-metal regime. Finally, its angle-dependent contribution was further investigated by plotting  $\alpha_{AHE}$  as a function of  $d$ . This result allowed a more elaborate theory curve of the angle-dependent AHE-contribution, that is in decent agreement for  $d \leq 45$  nm to the measured relative change of the MR in the oopj-plane, which enables to approximate the parameters  $\beta$  and  $\zeta$ . However, this improved theory curve still does not deliver any explanation for the measured increase in  $\left(\frac{\Delta\rho}{\rho}\right)$  for larger values of  $d$ , which supports the assumption of an additional contribution present in the thicker samples e.g. due to the presence of a crystalline order. So far the high conductivity regime has only been little investigated, so this experiment should be repeated with ferromagnetic conductors of a higher conductivity like Fe to receive more data in said regime. Additionally, further research needs to be conducted on the influence of the bandstructure on the intrinsic

mechanisms of the AHE.

The additional pure spin currents generated by the AHE hold great promise for future spintronics applications, as its flow direction and spin polarization can be controlled by changing the orientation of the magnetization with respect to the applied charge current [19, 37], which might find application in a large variety of spin-based devices. Recently Miron et. al. developed a device that can switch the magnetization in a ferromagnetic layer via the injection of charge currents [54]. An illustration of said device is given in Fig. 5.1.

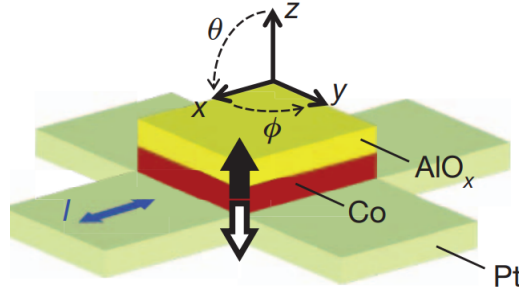


**Figure 5.1:** Scheme of the magnetization-switching device fabricated by Miron et. al.  $\text{AlO}_x$  and cobalt dots are deposited on top of a platinum Hall cross structure. Black and white arrows indicate the "up" and "down" magnetization states of the cobalt layer. A charge current along the  $x$ -direction gives rise to a spin current  $\mathbf{J}_s \parallel \mathbf{z}$  via the SHE, that is diffusing into the cobalt layer. The absorption of this polarized current is equivalent to a torque acting on the cobalt magnetization. Thus, the magnetization in the Co-layer can be switched by changing the current polarity. Its orientation is determined by measuring the Hall resistance,  $R_{\text{Hall}}$  along the transverse arm, which is proportional to the perpendicular component of the magnetization [54]. Taken from [54].

Miron et. al. used an NM-FM-interface with a charge-current driven through the nonmagnetic layer. Via SHE, it induces a spin current  $\mathbf{J}_s \parallel \mathbf{z}$ , that can enter the FM-layer and due to spin-orbit-torque (SOT) [55] influence and even switch its magnetization orientation based on the polarity of the current [54]. In this case, the AHE was used to determine the orientation of the magnetization by measuring the Hall resistance of the transverse arms  $R_{\text{Hall}}$ . We suggest a similar device to control the magnetization orientation based only on the AHE.

Looking at a system with two FMs (FM1 & FM2) connected by a NM, a charge current through FM1 in the right orientation to its magnetization  $\mathbf{M}_1$  could induce a spin current  $\mathbf{J}_s$  that can enter the NM and subsequently the FM2-layer and influence or even switch its magnetization  $\mathbf{M}_2$  orientation via SOT. The advantages of this device are, that it would, dependent on the orientation of  $\mathbf{M}_1$ , also allow to switch and align  $\mathbf{M}_2$  in-plane in contrast to Miron et. al. whose device only enables out-of-plane-switching. In future, a sample of this type needs to be fabricated to find out, whether and to what extent it can be used to control the alignment of  $\mathbf{M}_2$ .

Additionally, due to Onsager reciprocity, the AHE can in future also be used for electrical spin current detectors, where a spin current is transformed into a charge current [56, 57]. Last but not least, the recently discovered quantum anomalous Hall effect in topological insulators may open up an entirely new field for electronic devices, as it enables almost dissipationless charge and spin transport [58].

Lastly the ADMR-effects taking place in the bilayer of a ferromagnetic and a non-

magnetic conductor were investigated. For this purpose a sample containing 5 nm Pt deposited on top of 10 nm Co was fabricated. Upon conducting conventional ADMR-measurements under equal conditions to the previous ones, the magnitude of its AMR- and SMR-contributions were determined by calculating  $\left(\frac{\Delta\rho}{\rho}\right)$  in oopt and oopj-geometry and compared to the previous results of the FM-samples. By doing so, it was found, that the influence of the AMR-effect in oopt-geometry remained unchanged to previous results with the same layer thickness of Co, while a large increase in oopj- $\left(\frac{\Delta\rho}{\rho}\right)$  was visible due to the SMR. As expected, in in-plane alignment, the contributions of the AMR and SMR are added together.

In order to detect the USMR-effect, more sensitive ADMR-measurements with a decreased step-width, an increased digital filter count of 40 and a large current of  $I_0 = 25$  mA were conducted for both current polarities. To single out the even contributions of the USMR from the odd ones of the AMR and SMR, the differential voltage  $V_{\text{diff}}$  was calculated out of the measurement results of both polarities. The applied charge current led to a heating within the Hall-bar structure and a vertical thermal gradient  $\nabla T \parallel z$  that gave rise to additional voltage contributions caused by the SSE and ANE, whose angular dependence mimics that of the USMR. The differential electric field strength  $E_{\text{diff}}$  was calculated out of  $V_{\text{diff}}$  to remove the influence of the Hall-bar geometry. In transverse orientation only the effects caused by the thermal gradient are visible and therefore upon comparing the amplitude of its longitudinal and transverse angular change in value, the contribution of the USMR can be quantified. However no measurable difference in amplitude was found. Therefore it is assumed, that the thermal fluctuations that are present in the conventional Hall-bar geometry overshadow any possible USMR-effect, due to the large necessary charge current. By using Hall-bar-geometries with a smaller width  $w$ , a lower value of  $I_0$  is necessary to achieve the required current densities  $j$ , leading to less fluctuations within the data points. Consequently, these measurements should be repeated for similar samples with smaller Hall-bar geometries.

The USMR offers a variety of possible future applications. On the one hand it may lead to the fabrication of  $360^\circ$  directional sensitive AMR sensors, which could be used for magnetic field and current sensing measurements [49]. On the other hand, the USMR might enable the fabrication of two terminal spintronic devices, where switching of the magnetization can be caused by SOTs and its state can be read out by resistance measurements [48, 49].

To conclude, a lot of research in this field has to be done to ensure the mass production of the spintronics-based "Alpha Holo Core"-processor (Fig. 1.1) until 2035.

# Appendix A

## Details

### A.1 Bonding scheme

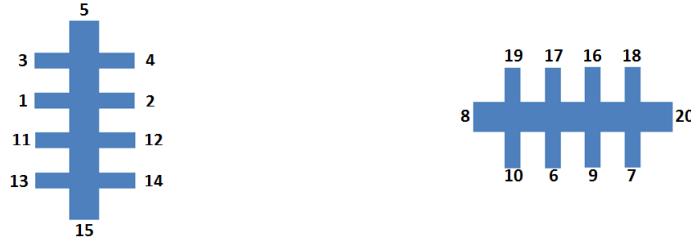


**Figure A.1:** Standard bonding scheme applied in this thesis.

### A.2 Hall-bar pads used for ADMR-measurements

Hall-bar	Measured quantity	Hall-bar pads
1 (vertical)	I	$5^+ - 15^-$
	$V_{\text{long}}$	$3^+ - 13^-$
	$V_{\text{trans}}$	$11^+ - 12^-$
2 (horizontal)	I	$8^+ - 20^-$
	$V_{\text{long}}$	$10^+ - 7^-$
	$V_{\text{trans}}$	$9^+ - 16^-$

**Table A.1:** Standard Hall pads used in ADMR-measurements-

### A.3 Fabricated samples

Layer thickness [nm]	Particularities
4 (3.6)	great difference in resistivity between the two Hall-bars
5 (4.5)	-
7 (6.3)	Hall-bar pat 13 broken. $V_{long}$ measured between $4^+$ and $14^-$
10 (9.0)	-
15 (13.5)	only one functioning Hall-bar
20 (18)	-
25 (22.5)	leftover material on horizontal Hall-bar
30-1 (27)	strangely high oopj-amplitude
30-2 (27)	-
35 (31.5)	-
40 (36)	-
50 (45)	-
65 (58.5)	-
80 (72)	damaged Hall-bar structure due to imperfect liftoff
100 (90)	-
120 (108)	-
10 (Co) +5 (Pt)	-

**Table A.2:** List of fabricated samples and particularities that occurred at their fabrication. Values in parenthesis are the actual layer thickness.

## A.4 Used abbreviations

SHE	spin Hall effect (see section 2.2.4)
ISHE	inverse spin Hall effect (see section 2.2.4)
AHE	anomalous Hall effect (see section 2.2.5)
AMR	anisotropic magnetoresistance (see section 2.3.3)
GMR	giant magnetoresistance [15]
TMR	tunneling magnetoresistance [16]
USMR	unidirectional spin Hall magnetoresistance (see section 4.3)
SMR	spin Hall manetoresistance (see section 2.3.1)
$\lambda_{sf}$	spin diffusion length
SOI	spin-orbit interaction (see section 2.2.1)
$\sigma$	specific conductivity (see section 2.2.1)
$\rho$	specific resistivity (see section 2.2.1)
$\alpha_{SH}$	spin Hall angle (see section 2.2.1)
OHE	ordinary Hall effect [30]
$\alpha_{AHE}$	anomalous Hall angle (see section 2.2.5)
ADMR	angle-dependent magnetoresistance effects (see section 2.3)
STT	spin-transfer torque [34]
NM	nonmagnetic conductor
FM	ferromagnetic conductor
FMI	ferromagnetic insulator
UHV	ultra-high vacuum
EVAP	electron-beam evaporation (see section 3.1.1)
Co	cobalt
Al	aluminium
Pt	platinum
PLD	pulsed laser deposition
Moria	Magneto-Optical-Resistance-Investigation-Apparatus (see section 3.2.1)
VTI	variable temperature insert (see section 3.2.1)
ip	in-plane geometry (see section 3.2.2)
oopj	out-of-plane geometry with $\mathbf{j}$ as rotational axis (see section 3.2.2)
oopt	out-of-plane geometry with $\mathbf{t}$ as rotational axis (see section 3.2.2)
SSE	spin Seebeck effect [51, 52]
ANE	anomalous Nerst effect [53]
SOT	spin-orbit torque [55]

**Table A.3:** Used abbreviations in order of their appearance.





## Appendix B

### Possible influence of a tilt on AMR-amplitude in oopj-geometry

In oopj-geometry, the sample can be tilted in the  $\mathbf{j}$ - $\mathbf{t}$ -plane, which can be described with a rotation around the  $\mathbf{z}$ -axis by the angle  $\alpha$  as well as in the  $\mathbf{n}$ - $\mathbf{j}$ -plane equal to a rotation around the  $\mathbf{y}$ -axis by the angle  $\gamma$ . Therefore the used oopj-magnetization vector

$$\mathbf{m}(\beta) = \begin{pmatrix} 0 \\ -\sin \beta \\ \cos \beta \end{pmatrix} \quad (\text{B.1})$$

must be multiplied by two rotation matrices, as defined in [59], to simulate the effects of a tilt in both  $\mathbf{j}$ - $\mathbf{t}$ -plane and  $\mathbf{n}$ - $\mathbf{j}$ -plane<sup>1</sup>:

$$\mathbf{m}_{\text{tilt}}(\alpha, \beta, \gamma) = R_z(\alpha)R_y(\gamma)\mathbf{m}(\beta) = \begin{pmatrix} \cos \alpha \sin \gamma \cos \beta + \sin \alpha \sin \beta \\ \dots \\ \dots \end{pmatrix} \quad (\text{B.2})$$

Inserting the  $\mathbf{j}$ -contribution of the tilted vector, the change in resistivity due to the AMR in oopj direction can be written as:

$$\rho_{\text{long}} = \rho_0 + \rho_1 \cdot m_{\mathbf{j}\text{-tilt}}^2 = \rho_0 + \rho_1 \cdot (\cos \alpha \sin \gamma \cos \beta + \sin \alpha \sin \beta)^2 \quad (\text{B.3})$$

As found in section 4.1.3, the maximum amplitude of the AMR in Co is approximately  $\left|\frac{\rho_1}{\rho_0}\right|=2.0\%$ .

Assuming this magnitude, it was found that a tilt of  $5^\circ$  in either of the both angles  $\alpha$  and  $\gamma$  gives rise to a  $\pi$ -periodical function that can be described as a  $\sin^2 \beta$ -function with an AMR-amplitude of  $\left|\frac{\rho_1}{\rho_0}\right|=1.5 \cdot 10^{-4}$ . These results are illustrated in Fig.B.1 and Fig. B.2 by simulating the behaviour of Eq. (B.3) in Mathematica and making use of its "Manipulate"-function to test the AMR-behaviour for varying values of  $\alpha$  and  $\gamma$ .

---

<sup>1</sup>Rotation matrices do not commute, hence  $R_z(\alpha)R_y(\gamma) \neq R_y(\gamma)R_z(\alpha)$ . Here their usual order  $R_z(\alpha)R_y(\gamma)$  is applied. The same procedure was also conducted for the order  $R_y(\gamma)R_z(\alpha)$ , however for the small applied values of  $\alpha$  and  $\gamma$  no changes in the resulting amplitudes were visible.

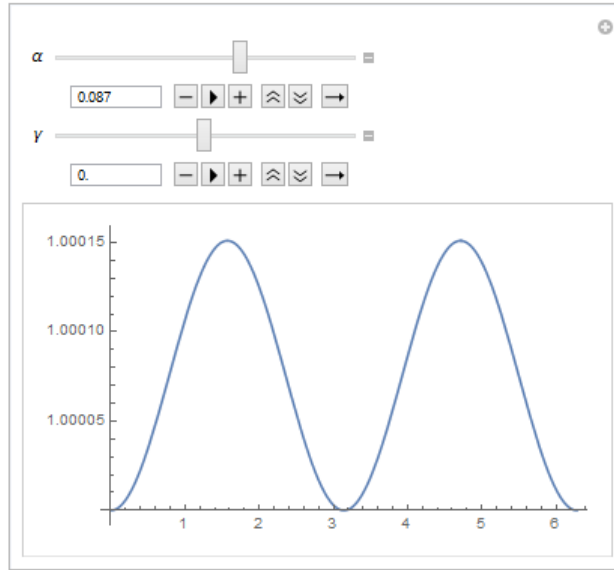


**Figure B.1:** Simulated oopj-behaviour for a tilt of  $\alpha = 0.087 \text{ rad} \approx 5^\circ$  with  $\rho_0 = 1$  and  $\rho_1 = 0.02$ . An amplitude of  $\left| \frac{\rho_1}{\rho_0} \right| = 1.5 \cdot 10^{-4}$  ensues.

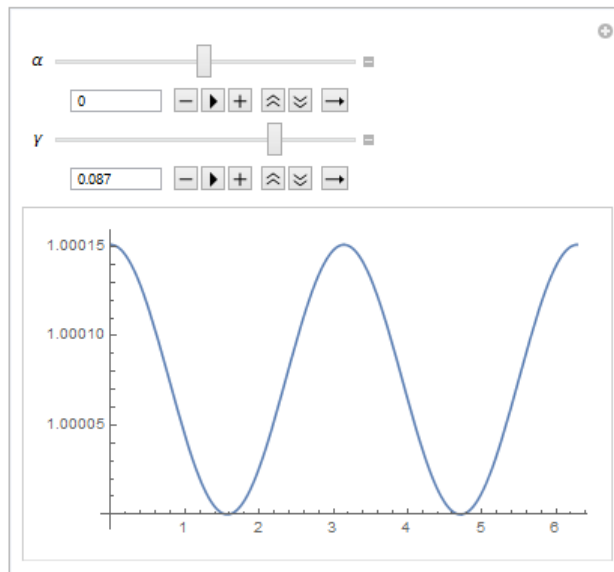


**Figure B.2:** Simulated oopj-behaviour for a tilt of  $\gamma = 0.087 \text{ rad} \approx 5^\circ$  with  $\rho_0 = 1$  and  $\rho_1 = 0.02$ . An amplitude of  $\left| \frac{\rho_1}{\rho_0} \right| = 1.5 \cdot 10^{-4}$  ensues.

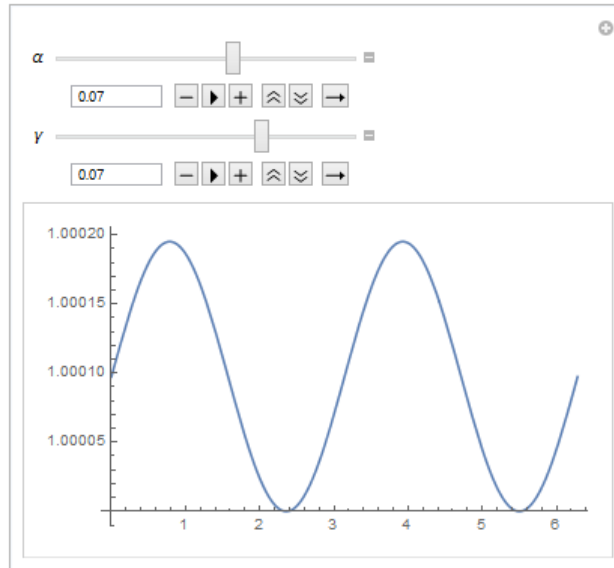


**Figure B.3:** Simulated oopj-behaviour for a tilt of both  $\gamma = 0.07 \text{ rad} \approx 4^\circ$  and  $\alpha = 0.07 \text{ rad} \approx 4^\circ$  with  $\rho_0 = 1$  and  $\rho_1 = 0.02$ . An amplitude of  $\left| \frac{\rho_1}{\rho_0} \right| = 2 \cdot 10^{-4}$  ensues.

In the course of this bachelor thesis it is assumed that a maximum tilt of  $\gamma = 4^\circ$  might have occurred due to imperfect glueing of the sample on the chip carrier, possible "sinking" effects during the bonding process where the bonding needle might have pressed the Si-plate further into the GE-glue and thereby changed the angle of  $\gamma$ , as well as unprecise placement of the chip carrier on the dipstick. During the glueing process it is also impossible to align the Hall-bars on the sample in a perfectly orthogonal  $\mathbf{j}$ - $\mathbf{t}$ -orientation. Therefore an additional maximum tilt of the angle  $\alpha = 4^\circ$  might have occurred. As depicted in figure (B.3), this leads to an assumed maximum contribution of a tilt on the oopj-amplitude of  $\left| \frac{\rho_1}{\rho_0} \right| = 0.02\%$ .



# Appendix C

## ADMR-results of the Co|Pt-sample

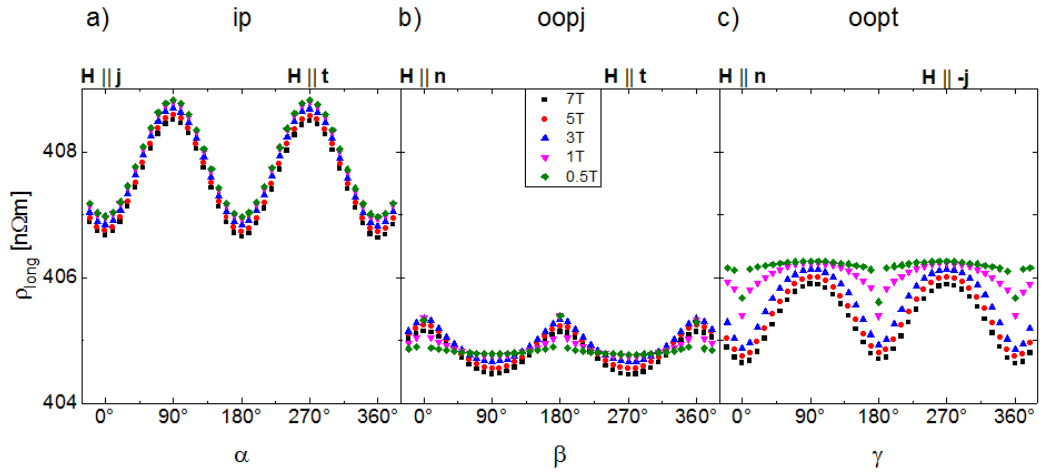


**Figure C.1:** Measured longitudinal ADMR behaviour of the resistivity of the Co|Pt-sample in each of the three possible measurement geometries for 5 different amplitudes of the magnetic field from 7 T to 0.5 T.

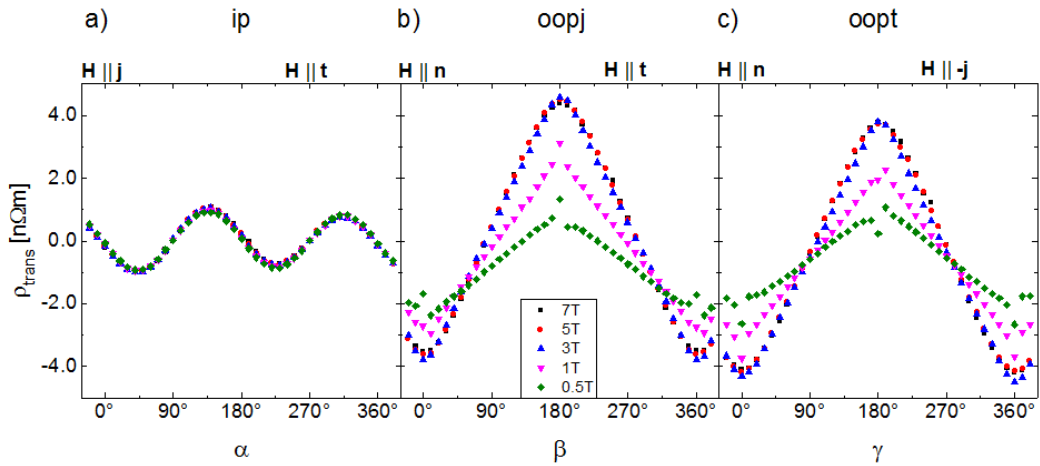


**Figure C.2:** Measured transverse ADMR behaviour of the resistivity of the Co|Pt-sample in each of the three possible measurement geometries for 5 different amplitudes of the magnetic field from 7 T to 0.5 T.



## Appendix D

### Application of the differential resistance $r$ to detect the USMR

As previously stated in section 4.3.3, the vertical temperature gradient  $\nabla T$  emerging in the Co|Pt-boundary layer at high values of  $I_0$  lead to an even higher order contribution of the current  $I$  to  $V$ .

$$V(I) = R(I)I + SI^2 \quad (\text{D.1})$$

Here  $R(I)$  is written to emphasize the current-polarity-dependence of the resistance  $R$ . According to Avcı et. al. it can be considered as a linear function of the current  $R(I) = R_0 + C \cdot I$  [49]. In order to receive  $R(I)$  out of the measurements of  $V(I)$ , its differential resistance  $r$  and curvature  $\kappa$  need to be determined.

$$r(\pm I) = \frac{dV}{dI} = R(\pm I) \pm (C + 2S)I \quad (\text{D.2})$$

$$\kappa(\pm I) = \frac{d^2V}{dI^2} = 2(C + S) \quad (\text{D.3})$$

The USMR-effect should be visible upon investigating the angular behaviour of  $r(I_0)$  and  $r(-I_0)$  by comparing their amplitudes at  $90^\circ$  and  $270^\circ$ . While one of them is enlarged at  $\alpha = 90^\circ$ , the other one is reduced. For  $\alpha = 270^\circ$  the reverse effect should be visible, with the formerly reduced  $r$  now being enlarged and vice versa. To determine the contributions of SSE and the ANE due to the thermal gradient  $\nabla T \parallel \mathbf{z}$ , that mimic the USMR-behaviour, the curvature  $\kappa$  needs to be calculated.

The mean differential resistance of the applied measurements<sup>1</sup> was determined by applying the following formula [60, 61]:

$$r(I_0) = \frac{1}{2} \left( \frac{V(I_0 + \Delta I) - V(I_0)}{\Delta I} + \frac{V(I_0) - V(I_0 - \Delta I)}{\Delta I} \right) \quad (\text{D.4})$$

In Fig. D.1, the longitudinal  $r$  is plotted as a function of the in-plane angle  $\alpha$ .

---

<sup>1</sup> $I_0=25.0$  mA,  $\Delta I=2.5$  mA.

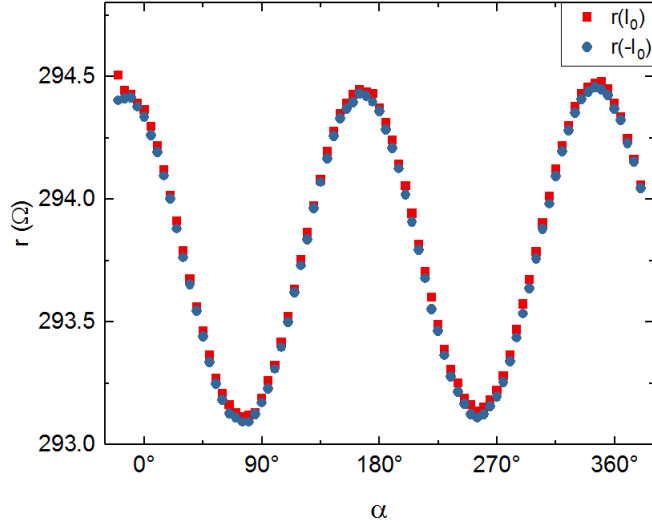


**Figure D.1:** Differential resistance of the Co|Pt-sample as a function of the angle  $\alpha$  for both current polarities.

As expected, the differential resistance depicts a  $\cos^2 \alpha$ -function due to the AMR, with slightly shifted offsets of  $r(I_0)$  and  $r(-I_0)$  due to the thermal contributions. However, the predicted angular dependence of the latter, leading to a difference in amplitude of  $r(I_0)$  and  $r(-I_0)$  at  $90^\circ$  and  $270^\circ$  is not visible.

In order to determine the curvature  $\kappa$ , and thus the contributions of the SSE and ANE, the following formula was applied [60, 61]:

$$\kappa(I_0) = \frac{1}{2} \left( \frac{V(I_0 + \Delta I) + V(I_0 - \Delta I) - 2V(I_0)}{\Delta I} \right) \quad (\text{D.5})$$

The resulting positive current polarity can be seen in Fig. D.2.

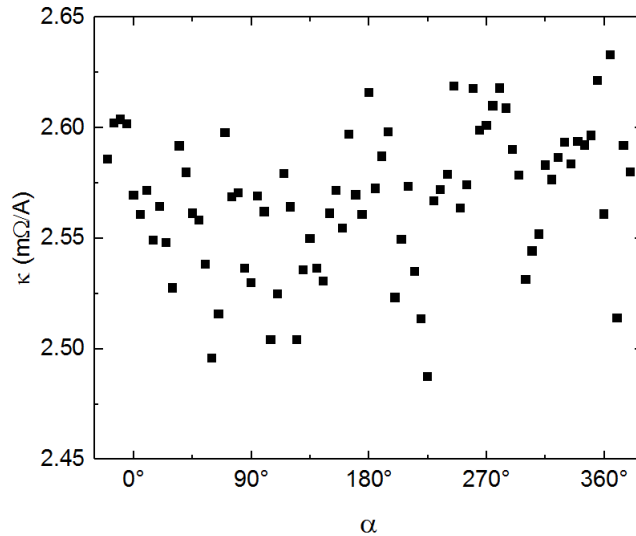


**Figure D.2:** Curvature  $\kappa$  of the Co|Pt-sample as a function of the angle  $\alpha$  for positive current polarity.

As one can see in Fig. D.2, the curvature  $\kappa$  of the voltage only contains noise, and



---

hence subtracting  $\kappa \cdot I_0$  from  $r$  does not deliver the desired resistance  $R(I)$ .

Just like in the method presented in section 4.3, the present fluctuations of the data points due to heat overshadow any possible USMR-effect as well as the contributions of the SSE and ANE. Furthermore, the range of  $\Delta I = 2.5$  mA might have been too large to determine the real values of  $r$  and  $\kappa$ . However, similar values were also conducted for lower values of both  $I_0$  and  $\Delta I$  delivering a similar noise result, as shown in Fig. D.2.



# Bibliography

- [1] *Murphy's take on Moore's law*, URL: <http://www.commitstrip.com/en/2015/08/28/murphys-take-on-moores-law/> (visited on 03/08/2017).
- [2] G. E. Moore, *Cramming more components onto integrated circuits*, *Electronics* **38**, 8 (1965).
- [3] *Intels Tick-Tack-Modell*, URL: <https://www.intel.de/content/www/de/de/silicon-innovations/intel-tick-tock-model-general.html> (visited on 03/08/2017).
- [4] M. Althammer, *Spin-transport-phenomena in metals, semiconductors, and insulators*, PhD thesis (Technische Universität München 2012).
- [5] L. B. Kish, *End of Moore's law: thermal (noise) death of integration in micro and nano electronics*, *Physics Letters A* **305**(3-4) (2002).
- [6] S. Meyer, *Spin Caloritronics in Ferromagnet/Normal Metal Hybrid Structures*, PhD thesis (Technische Universität München 2015).
- [7] S. A. Wolf, D. D. Awschalom, R. A. Buhrman, J. M. Daughton, S. von Molnár, M. L. Roukes, A. Y. Chtchelkanova and D. M. Treger, *Spintronics: A Spin-Based Electronics Vision for the Future*, *Science* **294**, 1488 (2001).
- [8] J. E. Hirsch, *Spin Hall effect*, *Physical Review Letters* **83**, 1834 (1999).
- [9] E. Saitoha, M. Ueda and H. Miyajima, *Conversion of spin current into charge current at room temperature: Inverse spin-Hall effect*, *Applied Physics Letters* **88**, 182509 (2006).
- [10] E. H. Hall, *On the Rotational coefficient in nickel and cobalt*, *Philosophical Magazine* **12**, 157 (1881).
- [11] S. Datta and B. Das, *Electronic analog of the electrooptic modulator*, *Applied Physics Letters* **56**, 665 (1990).
- [12] W. Thomson, *On the Electro-Dynamic Qualities of Metals:—Effects of Magnetization on the Electric Conductivity of Nickel and of Iron*, *Proceedings of the Royal Society of London* **8**, 546 (1857).
- [13] T. R. McGuire and R. I. Potter, *Anisotropic Magnetoresistance in Ferromagnetic 3d Alloys*, *IEEE Transactions on Magnetics* **11**, 1018 (1975).
- [14] R. Gross and A. Marx, *Festkörperphysik*, (Oldenburg, 2012).
- [15] G. Binasch, P. Grünberg, F. Saurenbach and W. Zinn, *Enhanced magnetoresistance in layered magnetic structures with antiferromagnetic interlayer exchange*, *Physical Review B* **39**, 4828 (1989).
- [16] J. S. Moodera, L. R. Kinder, T. M. Wong and R. Meservey, *Large Magnetoresistance at Room Temperature in Ferromagnetic Thin Film Tunnel Junctions*, *Physical Review Letter* **74**, 3273 (1995).
- [17] P. Grünberg, *Nobel Lecture*, 2007.
- [18] F. Czeschka, *Spin Currents in Metallic Nanostructures*, PhD thesis (Technische Universität München 2011).

- [19] M. Althammer, *Anomalous Hall Effect, Spin Hall Effect and Magnetoresistance*, Jülich Spring School (2017).
- [20] H. Haken and H. C. Wolf, *Atom- und Quantenphysik: Einführung in die experimentellen und theoretischen Grundlagen*, (Springer, 2004).
- [21] N. W. Ashcroft and N. D. Mermin, *Solid State Physics*, (Saunders College 1976).
- [22] J. Smit, *The spontaneous hall effect in ferromagnetics II*, Physica **24**(1-5), 39 (1958).
- [23] L. Berger, *Side-Jump Mechanism for the Hall Effect of Ferromagnets*, Physical Review B **2**, 4559 (1970).
- [24] N. F. Mott, *The Scattering of Fast Electrons by Atomic Nuclei*, Proceedings of the Royal Society of London **124**, 425 (1929).
- [25] S. Lowitzer, M Gradhand, Ködderitzsch, D. V. Fedorov, I. Mertig and H. Ebert, *Extrinsic and Intrinsic Contributions to the Spin Hall Effect of Alloys*, Physical Review Letters **106**(5), 056601 (2011).
- [26] A. Fert and P. M. Levy, *Erratum: Spin Hall Effect Induced by Resonant Scattering on Impurities in Metals*, Physical Review Letters **106**, 157208 (2011).
- [27] M. Gradhand, *The Extrinsic Spin Hall Effect*, PhD thesis (Martin-Luther-Universität Hall Wittenberg 2010).
- [28] N. A. Sinitsyn, *Semiclassical theories of the anomalous Hall effect*, Journal of Physics: Condensed Matter **20**, 023201 (2008).
- [29] D. Singh, *Spin Hall Magnetoresistance in Pt/ErFeO<sub>3</sub> – Hybrid Structures*, Bachelor's thesis (Technische Universität München 2016).
- [30] E. H. Hall, *On a new action of the magnet on electric currents*, American Journal of Mathematics **2**(3), 287 (1879).
- [31] N. Nagaosa, S. Sinova, S. Onoda, A. H. MacDonald and N. P. Ong, *Anomalous Hall Effect*, Reviews of Modern Physics **82** (2), 1539 (2010).
- [32] S. Onoda, N. Sugimoto and N. Nagaosa, *Quantum transport theory of anomalous electric, thermoelectric, and thermal Hall effects in ferromagnets*, Physical Review B **77**, 165103 (2008).
- [33] F. Witek, *Spin Hall Magnetoresistive Noise*, Master's thesis (Technische Universität München 2013).
- [34] M. Schreier, *Spin Transfer Torque mediated Magnetization Dynamics*, PhD thesis (Technische Universität München 2016).
- [35] Y.-T. Chen, T. Saburo, H. Nakayama, M. Althammer, S. T. B. Goennenwein, E. Saitoh and G. E. W. Bauer, *Theory of spin Hall magnetoresistance (SMR) and related phenomena*, Journal of Physics: Condensed Matter, **28** 103004 (2016).
- [36] M. Althammer, S. Meyer, H. Nakayama, M. Schreier, S. Altmannshofer, M. Weiler, H. Huebl, S. Geprägs, M. Opel, R. Gross, D. Meier, C. Klewe, J. -M. Kuschel T. Schmalhorst, G. Reiss, L. Shen, A. Gupta, Y. T. Chen, G. E. W. Bauer, E. Saitoh and S. T. B. Goennenwein, *Quantitative study of the spin Hall magnetoresistance in ferromagnetic insulator/normal metal hybrids*, Physical Review B **87**, 224401 (2013).
- [37] T. Taniguchi, J. Grollier and M.D. Stiles, *Spin-transfer torque in ferromagnetic bilayers generated by anomalous Hall effect and anisotropic magnetoresistance*, Proceedings of SPIE, Volume **9931**, 00310W (2016).

- [38] T. Taniguchi, *Magnetoresistance generated from charge-spin conversion by anomalous Hall effect in metallic ferromagnetic/nonmagnetic bilayers*, Physical Review B **94**, 174440 (2016).
- [39] R. Gross and A. Marx, *Lecture Notes on Spintronics*, (2005).
- [40] L. K. Zou, Y. Zhang, L. Gu, J. W. Cai and L. Sun, *Tunable angular-dependent magnetoresistance correlations in magnetic films and their implications for spin Hall magnetoresistance analysis*, Physical Review B **93**, 075309 (2016).
- [41] M. Díaz-Michelena, P. Cobos and C. Aroca, *Lock-in amplifiers for AMR sensors*, Sensors and Actuators A: Physical **222**, 149 (2015).
- [42] D. Irber, *Spin Hall-Magnetoresistance in FMI/NM/FMI-Trilayers*, Bachelor's thesis (Technische Universität München 2013).
- [43] S. C. Gelder, *Herstellung und Spin Hall Magnetwiderstand von Pt/ErFeO<sub>3</sub> Bilagen*, Bachelor's thesis (Technische Universität München 2015).
- [44] M. Althammer, *Magnetotransport measurement denitions at WMI*, (2017).
- [45] G. Fischer, H. Hoffmann and J. Vancea, *Mean free path and density of conductance electrons in platinum determined by the size effect in extremely thin films*, Physical Review B **22**, 6065 (1980).
- [46] J. T. C. De Vries, *Temperature and thickness dependence of the resistivity of thin polycrystalline aluminium, cobalt, nickel, palladium, silver and gold films*, Thin Solid Films Volume **167**, 25 (1988).
- [47] W. Limmer, J. Daeubler, L. Dreher, M. Glunk, W. Schoch, S. Schwaiger and R. Sauer, *Advanced resistivity model for arbitrary magnetization orientation applied to a series of compressive- to tensile-strained (Ga,Mn)As layers*, Physical Review B **77**, 205210 (2008).
- [48] C. O. Avci, K. Garello, J. Mendil, A. Ghosh, N. Blasakis, M. Gabureac, M. Trassin, M. F. Fiebig and P. Gambardella, *Magnetoresistance of heavy and light metal/ferromagnet bilayers*, Applied Physics Letters **107**, 192405 (2015).
- [49] C. O. Avci, K. Garello, A. Ghosh, M. Gabureac, S. F. Alvarado and P. Gambardella, *Unidirectional spin Hall magnetoresistance in ferromagnet/normal metal bilayers*, Nature Physics **11**, 570 (2015).
- [50] K. Olejník, V. Novak, J. Wunderlich and T. Jungwirth, *Electrical detection of magnetization reversal without auxiliary magnets*, Physical Review B **91**, 180402(R) (2015).
- [51] M. Weiler, M. Althammer, F.D. Czeschka, H. Huebl, M.S. Wagner, M. Opel, I. Imort, G. Reiss, A. Thomas, R. Gross and T. B. Goennenwein, *Local charge and spin currents in magnetothermal landscapes*, Physical Review Letter **108**, 106602 (2012).
- [52] T. Kikkawa, K. Uchida, Y. Shiomi, Z. Qiu, D. Hou, D. Tian, H. Nakayama, X. -F. Jin and E. Saitoh, *Longitudinal spin Seebeck effect free from the proximity Nernst effect*, Physical Review Letter **110**, 067207 (2013).
- [53] T. Kikkawa, K. Uchida, S. Daimon, Y. Shiomi, H. Adachi, Z. Qiu, D. Hou, D. Tian, X. -F. Jin, S. Jin, S. Maekawa and E. Saitoh, *Separation of longitudinal spin Seebeck effect from anomalous Nernst effect: Determination of origin of transverse thermoelectric voltage in metal/insulator junctions*, Physical Review B **88**, 214403 (2013).

- [54] I. M. Miron, K. Garello, G. Gaudin, P.-J. Zermatten, M. V. Costache, S. Auffret, S. Bandiera, B. Rodmacq, A. Schuhl and P. Gambardella, *Perpendicular switching of a single ferromagnetic layer induced by in-plane current injection*, Nature **476** 189 (2011).
- [55] Y. Fan, P. Upadhyaya, X. Kou, M. Lang, S. Takei, Z. Wang, J. Tang, L. He, L.-T. Chang, M. Montazeri, G. Yu, W. Jiang, T. Nie, R. N. Schwartz, Y. Tserkovnyak and K. L. Wang, *Magnetization switching through giant spin-orbit torque in a magnetically doped topological insulator heterostructure*, Nature Materials **13** 699 (2014).
- [56] B. F. Miao, S. Y. Huang, D. Qu and C. L. Chien, *Inverse Spin Hall Effect in a Ferromagnetic Metal*, Physical Review Letters **111**, 066602 (2013).
- [57] M. Wahler, N. Hommonay, T. Richter, A. Müller, C. Eisenschmidt, B. Fuhrmann and G. Schmidt, *Inverse spin Hall effect in a complex ferromagnetic oxide heterostructure*, Scientific Reports **6**, 28727 (2016).
- [58] C. -X. Liu, S. C. Zhang and X. -L. Qi, *The Quantum Anomalous Hall Effect: Theory and Experiment*, Annual Review of Condensed Matter Physics **7**(1), 301 (2006).
- [59] G. Fischer, *Lineare Algebra. Eine Einführung für Studienanfänger*, (Vieweg+Teubner , 2010).
- [60] P. D. Lax and M. S. Terrell, *Calculus with applications*, (Springer, 2013).
- [61] M. Ryan, *Calculus Essentials For Dummies*, (John Wiley & Sons, 2010).

# Acknowledgements

At this point, I want to thank all the people, who supported me and enabled this bachelor's Thesis. I would like to thank

- *Prof Dr. Rudolf Gross* for having offered me the opportunity to write my bachelor thesis at the Walter Meißner Institut für Tieftemperaturforschung (WMI).
- *Dr. Matthias Althammer* for his outstanding work as my supervisor. Despite his busy schedule, he always found time to answer my questions or help me out with the several problems I had with the UHV-Cluster as well as the Bonder. Furthermore his proofreading has greatly improved this thesis. Not to forget, his good advice with regard to my seminar talk was very helpful. I cannot thank you enough for the incredible amount of commitment you have invested in the making of this thesis.
- *Michaela Schleuder* for introducing me to the work processes in the clean room as well as volunteering to accompany me there on several occasions at the beginning of my work at the WMI, furthermore for giving me a lot of helpful advice.
- *Tobias Wimmer* for teaching me, how to thread the Bonder wire as well as helping me at the UHV-Cluster and in the cleanroom.
- *Dr. Stephan Geprägs* for his support concerning my questions about the UHV-Cluster.
- *Philip Schmidt* for helping me out during difficult liftoff processes as well as threading the Bonder wire for me.
- My fellow bachelor colleagues *Maxim Dietlein*, *Moritz Feil* and *Mirko Riedel* for the good atmosphere and for helping me out with several troubles.
- My mother *Heike Müller* for her proofreading of this thesis and my father *Michael Müller* for his support and sincere interest for my research. Additionally a special thank you and my grandfather *Dietrich "Eirik" Radspieler* for binding a printed version of this thesis for me.
- Lastly, I would like to thank all of the unnamed members of the Walther-Meißner-group for the good atmosphere and the great time I had working on this thesis.